Damage mechanisms assessment of Glass Fiber-Reinforced Polymer (GFRP) composites using multivariable analysis methods applied to acoustic emission data

W. Harizi, S. Chaki, G. Bourse, Mohamed Ourak

Version of Record: https://www.sciencedirect.com/science/article/pii/S026382232200263X
Manuscript_c4fd3787336096d4438408155a155888

Damage mechanisms assessment of Glass Fiber-Reinforced Polymer (GFRP) composites using multivariable analysis methods applied to acoustic emission data.

W. Harizi[a,*)], S. Chaki[b], G. Bourse[b], M. Ourak[c]

[a]*Université de Technologie de Compiègne, Roberval (Mechanics, Energy and Electricity), Centre de Recherche Royallieu, CS 60 319, 60203 Compiègne Cedex, France.*

[b]*Institut Mines-Télecom, IMT Nord Europe, Polymers and Composites Technology & Mechanical Engineering Department (TPCIM), CERI Matériaux et Procédés, 941 rue Charles Bourseul, CS 10838, Douai, F-59508, France.*

[c]*Université Polytechnique Hauts-de-France, Département d'Opto-Acousto-Electronique, IEMN, UMR CNRS 8520, Mont Houy BP 311, 59313 Valenciennes Cedex, France.*

[*)] *Corresponding author: walid.harizi@utc.fr*

Abstract

This work presents a coupling between three multivariable analysis techniques (Principal Component Analysis (PCA), K-means and Kohonen Self-Organizing Map (KSOM)) applied to the acoustic emission data recorded on Glass Fiber-Reinforced Polymer (GFRP) composite materials in order to monitor and identify, in real-time, their damage mechanisms: matrix cracking, interfacial debonding, fiber breakage and delamination between layers. Two mechanical loadings were used during this study: a monotonic tensile test until the failure and a step-wise tensile test of 50 MPa each time (7 ramps and 6 levels of 4 min holding time). The first loading, applied to the specimens in pure epoxy resin, unidirectional (UD) $[0]_4$ and $[90]_4$ GFRP, as well as the laminates $[0/90]_S$, allowed to evaluate the acoustic signature of each damage mechanism and establish a physical learning basis. The obtained physical data were employed for the learning operation of the Kohonen map which will be used for the identification of the damage mechanisms according to the level of the applied loading in the gradual tensile test. Post-mortem inspections conducted on the fracture facies of tested specimens under SEM confirmed the relevance of this {multivariable statistical analysis/acoustic emission} coupling for the detection and identification of GFRP damage mechanisms. Thus, the results of this study showed the relevance to identifying the damage mechanisms generated in a GFRP material by using multivariable acoustic emission analysis and provided a real potential for damage identification that would be developed in composite structures, made with the same material, under in-service loadings.

Keywords: Glass Fiber-Reinforced Polymer (GFRP); Acoustic Emission (AE); Damage mechanisms; Principal Component Analysis (PCA); K-means; Kohonen's Self-Organizing Map (KSOM).

1. Introduction

Polymer-matrix composite (PMC) materials present nowadays an exciting alternative to metallic materials conventionally used in industry [1–5]. PMCs bring many structural and functional advantages: mechanical resistance, lightness, electrical insulation and freedom of forms. Their growth is mainly linked to the transport industry development: aeronautics, aerospace, rail, naval and automotive. However, due to their heterogeneous, anisotropic and multilayer structure, their damage under mechanical stresses is a fairly complex phenomenon whose experimental characterization is far from being mastered despite the abundance of research works carried out on the subject for several years now [6–19]. In fact, the nature of the damage and the mechanisms behind its appearance and propagation are very different from those encountered in metallic materials. Likewise, inevitably, some defects can appear during the PMC manufacturing stage (lack of reinforcement, fiber misalignment, inclusions, porosities) and can have harmful consequences under service loadings [20–22]. Their shape, size, and distribution vary greatly depending on the PMC's nature and its manufacturing process. Under mechanical loading, four main damage mechanisms can occur in PMC materials: matrix cracking, interfacial debonding between fibers and matrix, fiber breakage and delamination between plies for the cross-ply laminated composites [5,6]. These damage modes are conditioned by the type of material architecture and the direction of applied mechanical stress. The damage begins at a microscopic scale, by the appearance of the matrix microcracks transverse to the stress direction, these microcracks propagate inside the material as the mechanical stress increases. They will generally be stopped by the fibers reinforcing the polymer matrix. At this level, several parameters are involved in the acceleration or slowing down of the damage process, such as the volume fraction, the reinforcement orientation, the ply thickness and mainly the stress direction. In fact, a high fraction of the fibers makes it possible to oppose the propagation of the microcracks if the fibers are oriented according to the loading direction. Also, a thin layer with a good inter-ply adhesion can increase the mechanical properties of the laminated composite. On the other hand, a mechanical stress perpendicular to the fiber orientation causes a gradual increase of the transverse microcracks and generates the pullout phenomenon of the fibers. The interfacial debonding occurs strongly if the bond quality between the fibers and their matrix is poor [6]. Thus, the transverse cracks can follow the interface path which, according to an energetic approach, is the easiest compared to that of fiber which has high mechanical properties. When the matrix cracks and fiber/matrix debonding propagate, the fibers become more and more the most loaded, they break one by one or packet by packet by resisting the loading and favoring a progressive rupture. The final failure of the PMC material is a combination and an accumulation of these various damage mechanisms [5].

Several non-destructive testing (NDT) techniques can be used to detect and quantify the PMC damage [23–25]. Acoustic emission (AE) is historically seen as one of the most effective methods to evaluate mechanical damage in PMC materials. It is defined as an energy release phenomenon in the form of transient elastic waves resulting from some local micro-displacements internal to a material subjected to stress [26]. The emitted elastic waves are initially ultrasonic volume waves (longitudinal and transverse), but undergo mode conversions, depending on the geometry of the tested structure, to transform into Lamb waves in the case of thin samples such as laminate composite structures. AE method consists of detecting these waves in order to extract real-time information on the material damage [27]. The bibliography is very abundant regarding the use of the AE technique for the damage characterization of PMCs. The synthesis in the chronological order of most of these works separates the analysis into two parts concerning the data processing mode: single-parameter or multiparameter analysis [28]. Conventional single-parameter processing of AE data considers a single

parameter among several to describe an acoustic signature corresponding to a specific damage mechanism. The parameters that can be used are numerous (amplitude, duration, rise time, counts, frequency, energy, etc.), which can be extracted directly from the temporal signal or its frequency spectrum. Most single-parameter studies use amplitude as a discriminating parameter of the damage mechanisms [6,7,18,28–31]. The amplitude describing the acoustic signatures varies from one test to another and from one study to another depending on the studied material, the used sensors, their coupling condition, the system and the threshold acquisition, etc. Therefore, it is very difficult to make a comparison between all of these studies. Despite the diversity of the studied composite materials and the conducted mechanical characterization tests, the amplitude criterion accords significant values to the fiber breakage and low values to the matrix cracking. However, a single damage mechanism, such as matrix cracking, can produce a wide range of amplitude. Indeed, several studies like [29,30] present some overlap intervals between two damage mechanisms, which does not allow the correlation with certainty between the AE amplitude and a particular damage mode. To solve these problems, the multivariable or multiparameter analysis has major advantages and more credibility. The authors attempted to analyze several descriptors of the AE signals. The AE descriptors can be temporal, frequency, time-frequency, etc. [32]. *Ely and Hill* [33] showed in the case of graphite/epoxy composite that the signals having the high characteristics (large amplitude, high energy, high number of counts and long duration) result from the breaking of fibers, but those having the weaker characteristics (low amplitude, low energy, low number of counts and short duration) result from longitudinal matrix cracks. *Barnes and Ramirez* [34], testing carbon fiber reinforced pipes, used at the same time the amplitude of the AE signals and their duration to characterize the different damage modes. They found a long duration and a low or medium amplitude (in the order of 45 to 70 dB) for the delamination and debonding, and for the breaking of fibers a high amplitude and short duration. However, the authors state that a damage mechanism such as matrix cracking can occur with a wide variation of the AE signal parameters. *Huguet and Godin* [28,35] used a parametric analysis for the classification of AE signals obtained for glass fiber/polyester matrix and glass fiber/epoxy matrix. For instance, *Huguet* considered six descriptors: amplitude, rise time, duration, energy, number of counts and number of counts during the rise time. This multivariable analysis is carried out using k-means, k-nearest neighbors and Kohonen self-organizing map (neural network) algorithms, which allowed separation of four different signal types A, B, C and D. Type A signals, linked to matrix cracks, are characterized by an amplitude comprised between 50 and 70 dB, a short duration, fairly slow rise time and relatively low energy. The signals type B have an amplitude between 70 and 100 dB, fairly short rise time and higher energies that are attributed to the interfacial debonding. Type C signals correspond to the fiber breakage, their rise and fall times are relatively short with fairly large amplitudes and energies. The fourth signal of type D describes fairly energetic signals, long durations, very slow rise time and covering a wide range of amplitude. *Huguet* attributes it to the delamination phenomenon between the plies of the studied PMC specimens. The choice of the most relevant descriptors to take into account for the classification can be made by visualization in Principal Component Analysis (PCA) diagram [32]. *Marec et al.* [32,36] used a Fuzzy C-Means (FCM) clustering associated with a principal component analysis. This last classification method is first applied to "simple" materials such as unidirectional (UD) composites. Then, more complex materials were studied: cross-ply composites, SMC (Sheet Molding Compound) composites and heterogeneous materials of polymer concrete type. The proposed classification method allows to take into account several parameters (number of counts at the peak, number of counts, energy and amplitude) that are used together in the same multidimensional analysis.

The number of AE hits detected during a mechanical loading is very large and complicated to process especially when several damage mechanisms happened, so it is necessary to use data

classification algorithms: the classifiers. A classifier is a mathematical method able to distribute the data, described by several parameters, into a finite set of classes with well-identified boundaries. In the AE method case, a classifier must allow the creation of a set of separate classes containing similar data describing the same damage mechanism in PMC material. Commonly, two types of classification algorithms exist: supervised and unsupervised. Supervised classification requires prior knowledge of the number of classes that we have. However, unsupervised classification is generally chosen where the classes are not known a priori by the user. It is rather interesting to choose the unsupervised approach while assuming that the operator does not have any information beforehand on the number of classes corresponding to damage mechanisms occurring in the studied material. The most used unsupervised classifiers for damage mechanisms discrimination in PMC materials are the K-means [28,35,37,38], K-Nearest-Neighbours [35,39], PCA [32,36,40] and the Kohonen self-organizing map [28,35]. The choice of pertinent AE descriptors, as the input database of these classifiers, is far from being mastered especially when applied to heterogeneous and anisotropic materials such as PMCs. In the analyzed literature, different choices of relevant descriptors are possible and each author argued his choice according to the case of study. *Huguet* [28] chose six descriptors to perform the multivariable statistical analysis: rise time, number of counts, energy, duration, amplitude and number of counts during the rise; while explaining that these parameters are the most used in the classical AE analysis. *Moevus et al.* [41] calculated the correlation matrix which connects 18 parameters describing the acoustic activity and established groupings according to their correlation coefficient "*r*". The determination of a threshold $r=0.8$ allowed the definition of the number of groups to be taken into account. It was chosen so as to select a subset of 8 parameters using a dendrogram representation. Each group of the most correlated entities is then described by only one of them because they provide the same acoustic information. However, the choice of threshold value remains questionable. *Marec* [36] selected the most relevant descriptors using the PCA method. It was carried out on the data obtained on a 45°UD Glass Fiber-Reinforced Polymer (GFRP) composite that was submitted to a tensile test. The descriptors were illustrated in the 2D plane corresponding to the two principal components with the highest variances. In this case of study, the number of counts at the peak, the number of counts, the energy and the amplitude gave a PCA with less overlap and were thus selected as the appropriate descriptors.

The current study leads with the use of the AE method for detection and monitoring of the damage mechanisms of UD $[0]_4$, $[90]_4$ and cross-ply $[0/90]_S$ E-GFRP laminates subjected to various mechanical loads: monotonic tensile until failure and step-wise tensile test. The use of the multivariable analysis algorithms, in particular the coupling between PCA and K-means, will allow the elimination of redundant AE descriptors. Firstly, the objective will be to carry out some typical AE tests allowing us to identify the various damage mechanisms according to their acoustic signature. To do, simple specimens of a pure epoxy matrix, then UD GFRP samples at 90° and 0° were submitted to uniaxial tensile test to determine, respectively acoustic signatures of matrix cracking, interfacial debonding between fiber and matrix, fiber breakage. Cross-ply composites $[0°/90°]_S$ will be studied to identify the delamination signature. Then, it is possible to practice the labeling Kohonen map, which will allow the various AE events to be grouped on classes, each one corresponding to a damage type. Kohonen map can now be used to characterize the damage of a healthy laminated $[0/90]_S$ specimen under monotonic tensile test with successive holding stages. The obtained damage mechanisms classification will be validated with fractographic observations using Scanning Electron Microscopy (SEM).

2. Used unsupervised analysis methods

Used data classification methods are mainly based on the concept of vectors and the calculation of the Euclidean distance. Once the pertinent descriptors are selected, experimental data is represented in the form of vectors forming a global matrix $\boldsymbol{X}$ of n rows and d columns (Eq. (1)). The n rows are the observation numbers and the d columns are the parameter numbers describing each observation. In order to homogenize all the data, it is interesting to transform them into reduced centered variables. Thus, each column of the matrix $\boldsymbol{X}$ has a zero mean and a standard deviation equal to unity (centering a variable consists of subtracting its mean from each of its initial values and reducing it consists of dividing all its values by its standard deviation). If x_1^j et x_2^j ($j=1,d$) are two observations (two vectors lines) of the input matrix $\boldsymbol{X}$, the usual Euclidean distance $d(x_1^j, x_2^j)$ is calculated according to Eq. (2).

$$\boldsymbol{X} = \begin{bmatrix} x_1^1 & x_1^2 & \dots & x_1^d \\ x_2^1 & x_2^2 & \cdots & x_2^d \\ \vdots & \vdots & \vdots & \vdots \\ x_n^1 & x_n^2 & \cdots & x_n^d \end{bmatrix} \quad \textbf{(1)}$$

$$d(x_1^j, x_2^j) = \sqrt{\sum_{j=1}^{d} (x_1^j - x_2^j)^2} \quad \textbf{(2)}$$

2.1. K-means method

It is one of the most used classification algorithms due to its implementation simplicity. K-means is an iterative method, with "mobile centers", which consists of partitioning data by the concept of minimizing intra-group variance [28]. The coordinates of the group centers are initialized randomly or manually. Then, each input vector x_i^j ($i=1,n$ and $j=1,d$) is assigned to the nearest group, depending on the Euclidean distance (Eq. (2)) between the input entity x_i^j and the group centers G_I^j ($I=1,K$ with K is the number of groups and $j=1,d$). Then, by randomly changing the coordinates of the centers, the procedure is repeated until no change in the coordinates of the centers is reported, at this stage, the algorithm converges [32].

2.2. Principal component analysis (PCA)

One of the major inherent difficulties of multidimensional statistics is the problem of data visualization. Indeed, as soon as there are more than three variables, it is more difficult to visualize them. On the other hand, some variables are generally correlated in the dataset because of redundancy in carried information, so the problem can be simplified by replacing the group of linked variables with a new variable. PCA is a quantitative method to achieve this simplification. This method generates a new set of variables, called principal components. Each principal component is a linear combination of the input variables (original variables forming the matrix $\boldsymbol{X}$). Seen that all the principal components are orthogonal, there is no redundancy of information. Commonly, the sum of the variances of the first principal components exceeds 80% of the total variance of the original data.

The covariance matrix $\boldsymbol{C_x}$ of $\boldsymbol{X}$ can be calculated according to the Eq. (3) where t represents the transpose of the matrix and $E[\ \ ]$ its mathematical expectation.

$$C_x = E[\boldsymbol{X}\boldsymbol{X}^t] \quad \textbf{(3)}$$

The components of $\boldsymbol{C_X}$, denoted C_{kl} ($k=1,d$ *et* $l=1,d$), represent the covariances between the variables x^k et x^l:

$$x^k = \begin{bmatrix} x_1^k \\ x_2^k \\ \vdots \\ x_n^k \end{bmatrix}, \qquad x^l = \begin{bmatrix} x_1^l \\ x_2^l \\ \vdots \\ x_n^l \end{bmatrix} \tag{4}$$

As the covariance matrix is symmetric, an orthogonal basis can be calculated by finding its eigenvalues and eigenvectors. The eigenvectors e_k and the corresponding eigenvalues λ_k are the solutions of the Eq. (5).

$$C_x e_k = \lambda_k e_k, \qquad k = 1,2, \dots d \tag{5}$$

The eigenvalues obtained from Eq. (5) correspond to the variances of the principal components. An ordered orthogonal basis can be created with the first eigenvectors having the direction of the largest variances of the data. Thus, directions in which the data set has the most significant amounts of energy can be found. Instead of using all the eigenvectors of the covariance matrix, the data will be represented in terms of only a few basis vectors of the orthogonal basis. If $\boldsymbol{A_Z}$ ($d \times Z$) is the matrix having the first Z eigenvectors, by transforming the data $\boldsymbol{X}$, Eq. (6) can be obtained representing the new coordinates of the n observations in the orthogonal coordinate system defined by the eigenvectors.

$$y = \boldsymbol{X A_Z} \tag{6}$$

2.3. Kohonen self-organizing map (KSOM)

Kohonen map is a neural network based on the same topological properties of the human brain known as a map of self-organizing entities. This type of network belongs to the category of unsupervised methods. The main characteristic of this algorithm is its ability to develop entities corresponding to the distributions of the input vectors and to organize them in a consistent and topological manner. KSOM is inspired by the human nervous system according to two fundamental points:

- Knowledge is acquired through a learning process,
- The weights of the connections between the neurons are used to memorize the knowledge.

KSOM neurons are distributed in a single layer in which the neighborhood notion is of particular interest. There are three types of topology: a rectangular (**Fig.1**a), hexagonal (**Fig.1**b) and random (**Fig.1**c) map of neurons. Each neuron q has a weight vector W_q. The input vector x_i^j ($i=1,n$ and $j=1,d$) of the matrix $\boldsymbol{X}$, comprising n observations (n AE hits) described by d pertinent descriptors (d variables), is unique and common to all neurons of the network.

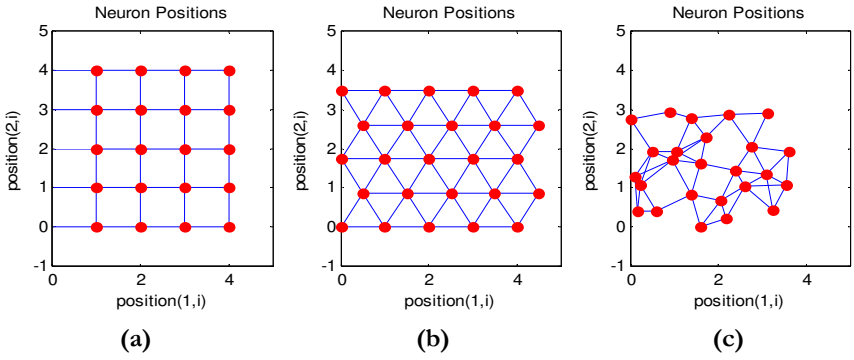

Fig.1. Different topologies of KSOM: (a) rectangular, (b) hexagonal and (c) random topologies [42]

This unsupervised method requires a learning phase comprising the five following steps:

(1) Initialization of the weight vectors W_q by assigning them the average values of the input database $\boldsymbol{X}$ (the averages of the columns of the matrix $\boldsymbol{X}$),

(2) Introduction of an input vector x_i^j at the input of the network,

(3) Research of the winning neuron noted q^*; it is the neuron whose weight vector W_{q^*} is closest to the input vector x_i^j, by measuring the Euclidean distance using Eq. (2),

(4) Adaptation of the weight of this winning neuron as well as those of its topological neighbors so that they are close to the input vector x_i^j according to Eq. (7),

$$W_q(t+1) = W_q(t) + \eta N(q^*)\left(x_i^j - W_q(t)\right) \quad if\ \mathrm{q} \in N(q^*)$$
$$W_q(t+1) = W_q(t) \quad if\ \mathrm{q} \notin N(q^*) \tag{7}$$

$N(q^*)$ is the neighborhood of the winning neuron, η is the learning rate and t represents the iteration number.

A rectangular topology of 10×10 neurons is shown in **Fig. 2**. Once the winning neuron (Home neuron) is selected, the neighborhood radius changes from 1 for "*neighborhood 1*" to 2 for "*neighborhood 2*" until it reaches 3 for "*neighborhood 3*". The neighborhood radius can be fixed during the learning phase, or increased at the start and then decreased depending on the number of iterations.

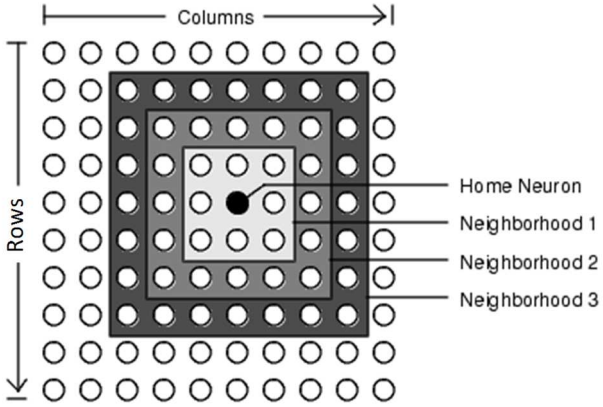

Fig. 2. The neighborhood of a winning neuron in the case of rectangular topology [42].

(5) Repetition of the previous steps for all line vectors forming the global matrix $\boldsymbol{X}$ according to a certain number of iterations.

A gain must be defined, balancing the learning with each passage of an input vector, which decreases as iterations. Learning ends when the weights converge (very close to the inputs vectors) or the gain becomes close to 0.

After inputting all vectors, the neurons will be organized topologically so that nearby neurons correspond to similar input vectors. Once learning is complete, the map can be used to classify new data that was not used for the learning operation.

3. Materials and experimental procedures

3.1. Tested materials: pure epoxy resin, UD and cross-ply E-glass fibers/epoxy laminate specimens

Four specimen types were manufactured in: (1) pure resin, (2) UD $[90]_4$ E-glass fibers reinforced epoxy resin at 90° to the mechanical stress direction, (3) UD $[0]_4$ E-glass fibers oriented at 0° in the epoxy matrix and (4) cross-ply $[0/90]_S$ composite laminates.

3.1.1. Pure resin specimens

They were made from a resin/hardener mixture of the "EPOLAM 5015" type from AXSON. This epoxy resin, with a low viscosity of 0.2 Pa.s, allows a good impregnation of the fibrous reinforcement. The mixing proportions are presented in **Table 1**, according to the manufacturer's technical sheet.

Table 1. Physical properties of the EPOLAM 5015 resin and hardener used for the manufacturing of the pure resin samples

Physical properties		
	EPOLAM 5015 resin	**EPOLAM 5015 hardener**
Mixing ratio (weight)	100	30
Aspect	liquid	liquid
Color	Light amber	colorless
Density at 25°C (g/cm^3)	1.15	0.93
Glass transition temperature (°C)	80	

The mixture was poured into an open mold having 290×290×3.5mm^3 in dimensions and was kept for 24 hours at a temperature of 23°C. Once hardened, it was placed in an oven for 2 hours at 80°C and then demolded. The final polymerized product has a density of 1.10 g/cm^3 and was used to produce the test samples (with 250×20×3.5mm^3 in dimensions) for mechanical characterization (**Fig. 3**a).

3.1.2. UD and cross-ply GFRP specimens

The tested composite materials were two UD ($[0]_4$ and $[90]_4$) and one cross-ply $[0/90]_S$ laminates consisting of E-glass fibers and epoxy resin. The fiber volume fraction of the laminate composites was 54% as prepreg sheets with uncured epoxy. Heels were integrated to the plates before curing in order to create tensile test specimens, as shown in **Fig. 3**b. They were built by a twill tape 2/2, with ±45° oriented fibers, placed on the outer of the stack according to the ISO 527-5 standard [43]. A compression molding process (at 120 °C for 60 min) was used in this study to obtain, as far as possible, planar plates with uniform thickness. All tensile specimens were cut from the same plate to reduce the variability of the material properties. Tensile specimen dimensions are shown in **Fig. 3**a (for resin pure), **Fig. 3**b (for UD and cross-ply laminates) and detailed in **Table 2**.

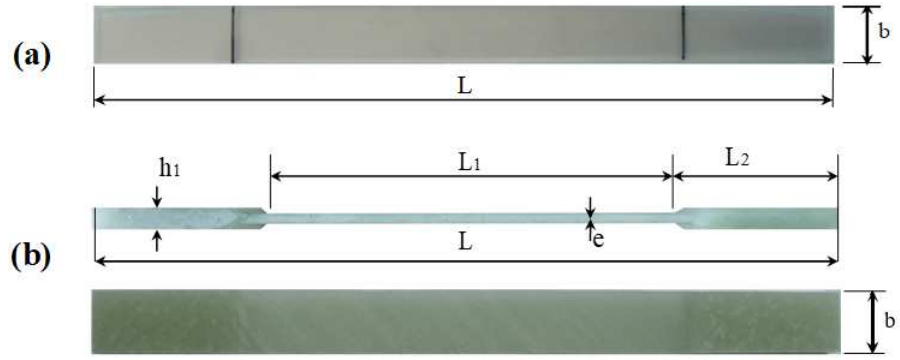

Fig. 3. (a) Pure resin samples; (b) UD and cross-ply GFRP specimens.

Table 2. Dimensions of the test specimens used for the mechanical characterization

Symbols	**Designation**	**Values (mm)**
L	Total length	250
L_1	Distance between heels	150±1
L_2	Length of heels	≥ 50
b	Width	20±0.5

e	Thickness of the specimen	3.5±0.2
h_1	Thickness of the heels	7.5

3.2. Mechanical loadings and experimental device

The first loading (loading (1) in **Fig.4**a) consists of a monotonic tensile test until failure. It is used for the generation of the desired damage mechanism, according to the type of tested sample, and thus identification of its acoustic signature. To do this, simple samples (pure resin and UD GFRP specimens), whose damage mechanisms are relatively easy to highlight, are firstly tested, then at the end the cross-ply $[0/90]_S$ samples. This method consists in identifying with a staggered manner the different AE signatures of the damage mechanisms. We start with the identification of the isolated matrix cracking in the tested pure resin specimens; their acoustic emission signals will be noted "**A**". In the UD $[90]_4$ GFRP samples, a second acoustic signature will be identified and related to the fiber/matrix debonding (signals "**B**"). This second identification is possible by deduction since the matrix cracking signature is already known. The signature of the fiber breakage is identified on UD $[0]_4$ specimens, where the fibers are oriented in the same direction of the mechanical stress, by separating it from the signals A and B. The signals corresponding to fibers rupture will be noted "**C**". Knowing the three signatures (A, B and C), the identification of the fourth one "**D**" linked to delamination between the plies of the laminate cross-ply $[0/90]_S$ samples finally becomes possible. This methodology is presented in the tree structure form in **Fig.4**b.

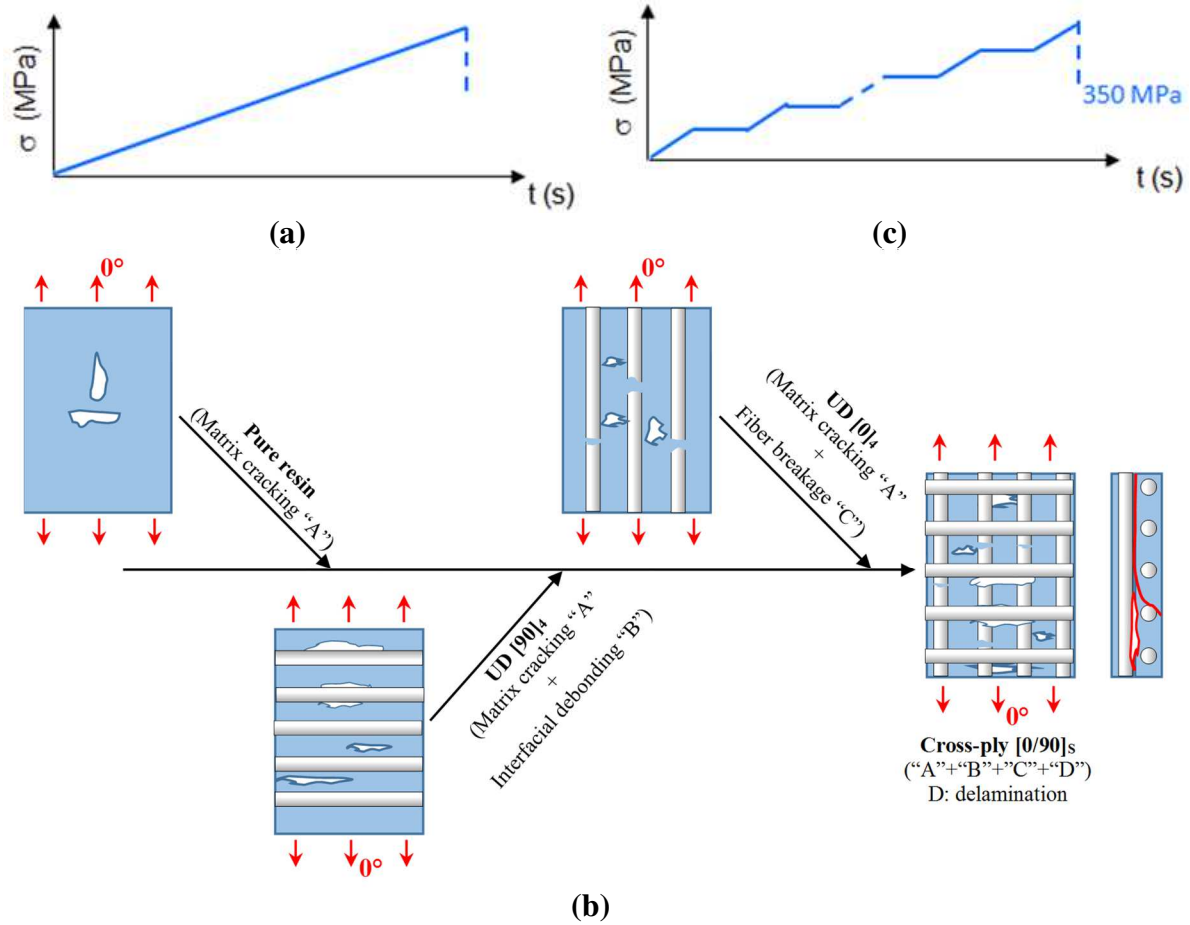

Fig.4. (a) Loading (1): monotonic tensile test; (b) The staggered identification of AE signatures using loading (1); (c) Loading (2): a step-wise static tensile test of 50 MPa loading ramps.

Since the identification of all signatures is achieved, now it is possible to practice the labeling of Kohonen's map, which will allow grouping the various AE events according to classes, each corresponding to a damage type. After that, KSOM will be used to identify the damage mechanisms created in healthy cross-ply $[0/90]_S$ samples under tensile loading. As an application of this approach, the last samples were submitted to a step-wise tensile test of 50 MPa loading ramps (7 ramps and 6 levels of 4 min holding time, (loading (2) in **Fig.4**c)) in order to identify created damage mechanisms during each stage of loading (2). **Fig.5** summarizes the adopted approach for the damage characterization during the two mechanical loadings (1) & (2).

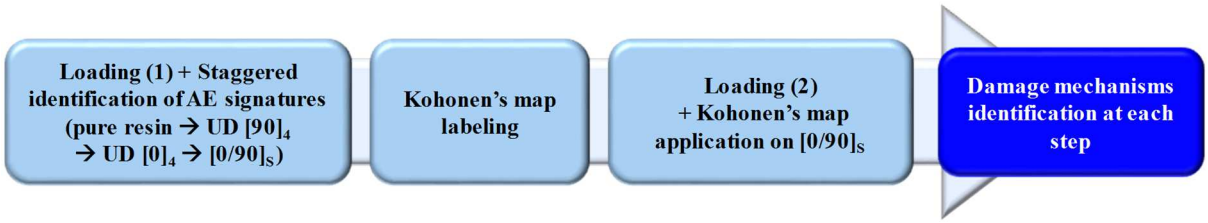

Fig.5. Adopted approach during the two mechanical loadings (1) & (2).

These two mechanical loadings were performed at a cross-head speed of 0.5 mm/min using an electrical tensile machine (INSTRON 1185) with a load cell of 100kN (**Fig.6**). An extensometer with a gauge length of 10 mm is attached to the specimen surface to measure the elongation. Two AE sensors (Nano-30, 125-750 kHz, from Physical Acoustics Corporation-MISTRAS Group), connected to a 40 dB pre-amplification, were coupled with silicone grease on the same face of the sample. They are symmetrically arranged from the center of the specimen length with a distance of 120 mm between them. Furthermore, these sensors are related to an AE acquisition and processing system (DiSP with 8 acquisition channels of 16 bits [44]).

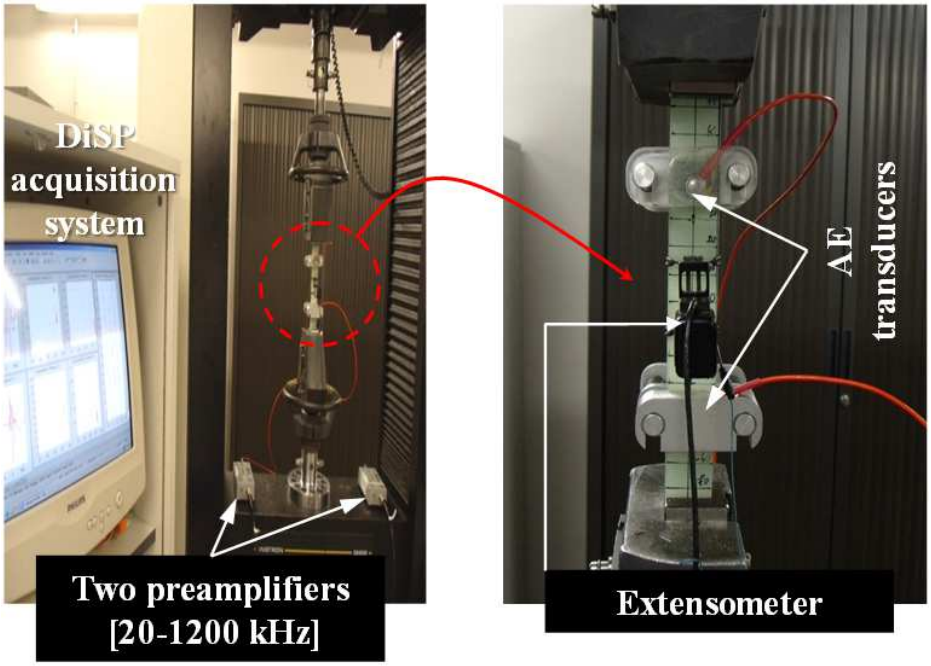

Fig.6. Experimental device used for the AE tests during the two mechanical loadings.

The acquisition threshold is determined when the specimen is clamped between the two jaws of the tensile machine and at zero stress. For each specimen type, the acquisition threshold was

increased step by step in such a way as to avoid the acquisition of any acoustic activity coming from the external environment outside of the test specimen (surrounding background noise). It turned out that a threshold of 34 dB was sufficient to avoid acquiring acoustic activity from outside the pure resin specimens. This threshold was a little higher for the UD and cross-ply GFRP specimens where their value was optimized and reached 38 dB. This difference in acquisition thresholds between the pure resin and composite specimens is due especially to the presence of heels on the composite specimens and their absence on the pure resin ones. Having heels on both sides of the composite specimens allows a slightly higher tightening at the two jaws level of the tensile machine and thus could generate an acoustic activity increasing the acquisition threshold at zero stress. The three time windows for AE signal measurement were chosen as follows: PDT = 50 µs (Peak Definition Time), HDT = 100 µs (Hit Definition Time) and HLT = 300 µs (Hit Lockout Time).

3.3. Determination of the pertinent AE descriptors by coupling PCA and K-means methods

In our case, the AE data can be represented by a matrix $\boldsymbol{X}$ of $n \times 13$ dimensions, where n is the number of hits, which depends on the type of tested sample and its acoustic emissivity. Each hit can be described with thirteen variables (or descriptors) defined in [44] as: rise time, counts to peak, counts, duration, amplitude, energy, absolute energy, average frequency, ASL (Average Signal Level), RMS (Root Mean Square), reverberation frequency, initiation frequency and signal strength. In principal component analysis (PCA), by retaining the first two (or three) principal components corresponding to the highest variances, the original data can be projected into a new 2 (or 3) dimensional space. Thus, the descriptors are correlated with these new axes of projection. Among the thirteen descriptors, several provide the same information. Partially, this can be explained by the mathematical relationships connecting some descriptors [44]. Beyond these direct connections, the most relevant descriptors would be objectively determined when applying simultaneously k-means and PCA algorithms on all thirteen variables. Two conditions are defined for a variable to be selected as a relevant descriptor:

• **1st condition**: the fact of deleting it results in a loss of information, which automatically changes the result of the classification by k-means.

• **2nd condition**: in the representation in principal components, the vector associated with a relevant variable must be distinct (length, direction) from the other vectors previously selected.

In order to objectively apply the k-means algorithm for selecting the pertinent variables, Davies and Bouldin criterion, called *DB,* was used to define the number of classes existing in a dataset. DB criterion is defined by Eq. (8) where d_i and d_j are the averages of the Euclidean distances within the class of groups i and j, respectively. D_{ij} is the distance between the two groups i and j.

$$DB = \frac{1}{K}\sum_{i=1}^{k} max_{i \neq j}\left\{\frac{d_i + d_j}{D_{ij}}\right\} \quad \textbf{(8)}$$

The determination of the relevant descriptors is carried out from the AE data recorded on the UD $[90]_4$ GFRP samples (this is the most unfavorable configuration for the propagation of the acoustic waves because the glass fibers are oriented perpendicular to the line connecting the two AE sensors). The number of classes K minimizing the calculated *DB* coefficient based on the data in each UD $[90]_4$ sample is equal to 2, confirming the existence of two damage mechanisms for this configuration of the studied GFRP material (**Fig.7**a). Thus, the k-means algorithm is applied on the reduced centered experimental database, with a classes number equal to 2 and a maximum number of AE descriptors equal to 13. **Fig.7**b illustrates two clusters (classes) of the percentage of 98.75% and 1.25%, respectively.

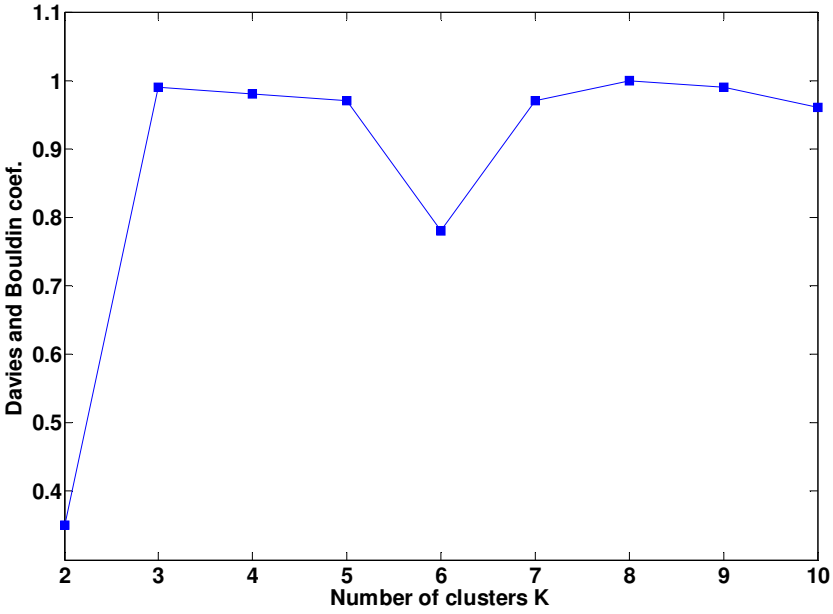

(a)

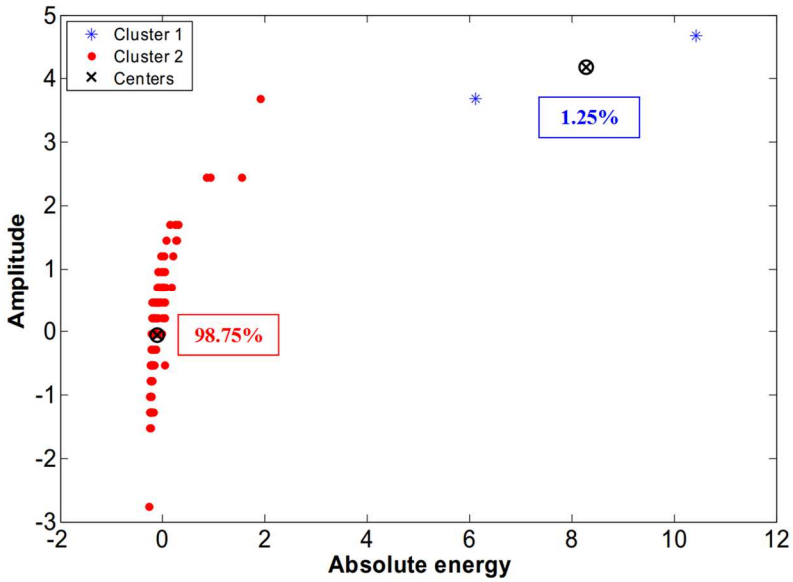

(b)

Fig.7. (a) Evaluation of the *DB* coefficient; (b) k-means application on the experimental AE data recorded on a UD $[90]_4$ sample.

The thirteen variables are projected onto the first two principal components and are represented in **Fig.8** in the form of vectors (blue, purple and green lines). The red dots are the original data of the input matrix ***X*** represented in this new two-dimensional coordinate system.

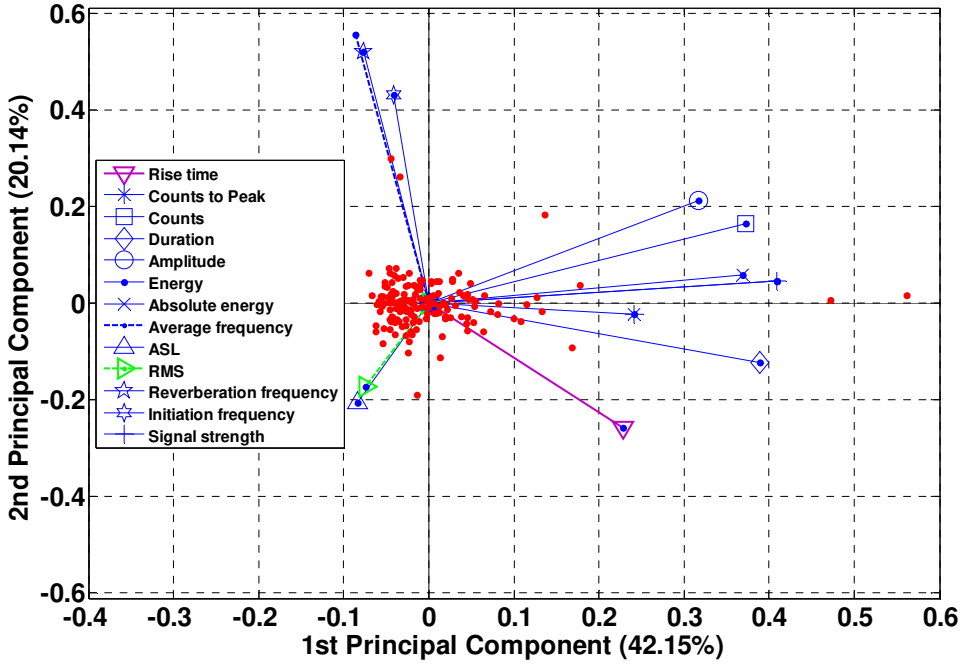

Fig.8. PCA visualization of the contributions of the 13 AE descriptors on the two first principal components: the first component has a variance of 42.15% and the second is of the variance of 20.14% compared to the total variance.

When applying the two selection conditions of the relevant descriptors, delete of the variables {ASL, RMS, the reverberation frequency, the initiation frequency, the signal strength and the average frequency} did not modify the classification result obtained by k-means (98.75% and 1.25%). Thus, the last result allows using of just 7 variables instead of 13.

The PCA application based on the seven remaining descriptors (**Fig.9**) shows that the rise time and the number of counts to the peak are fairly correlated. They provided the same information on the AE data, so only one of them is sufficient; the rise time is chosen. The five remaining descriptors are placed in the same lower right part, which explains the existence of a correlation between them. Indeed, the number of counts and the duration are two descriptors close to each other (the number of counts is the number of exceeded thresholds during the duration of the hit); thus the number of counts is selected. Concerning the three remaining descriptors (amplitude, energy, absolute energy), only the energy removal did not change the classification result (condition 1). Thus, the PCA and k-means coupling allowed us to select rise time, number of counts, amplitude and absolute energy as being the four pertinent descriptors with the least possible recovery. This approach has been validated for all the studied GFRP samples.

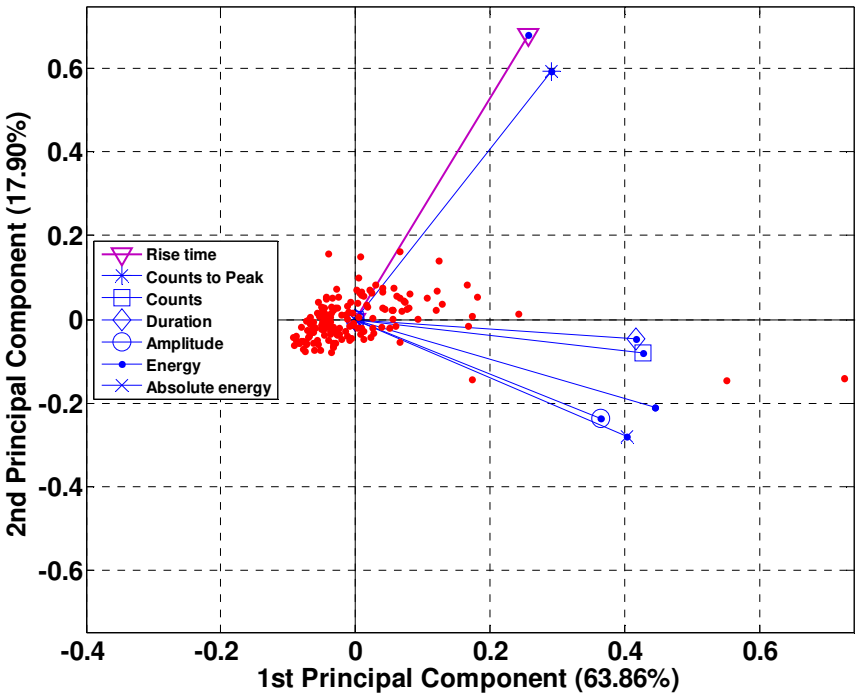

Fig.9. PCA visualization of the contributions of the 7 remaining descriptors on the two first principal components: the first component has a variance of 63.86% and the second one has a variance of 17.90% compared to the total variance.

4. Results and discussions

4.1. Acoustic signatures identification during loading (1)

4.1.1. Mechanical and acoustic coupling on the pure resin and UD configurations

a. Pure resin samples

Fig.10a illustrates the typical mechanical behavior in the monotonic tensile test until the failure of pure resin samples (curve in a continuous black line), coupled with the amplitude of their acoustic emission activity (blue dots). From 0.22% strain, the matrix cracking appears and it will lead to the sample rupture for a strain of 1.55%. The amplitude of the recorded acoustic emission is understood between 34 dB (acquisition threshold) and 50 dB. **Fig.10**b shows the hit waveform type "A" characterizing the matrix cracking from an acquisition threshold (red lines) set at 34 dB, which corresponds to a voltage of ±5 mV. The four relevant descriptors (rise time, number of counts, amplitude and absolute energy) selected in section 3.3, characterizing this signal type, are presented in **Table 3** as average values over all of the recorded hits on five samples.

Table 3. Average values of the recorded hits on five pure resin samples during loading (1)

Rise time (µs)	Counts	Amplitude (dB)	Absolute energy (aJ)
6	5	41	12

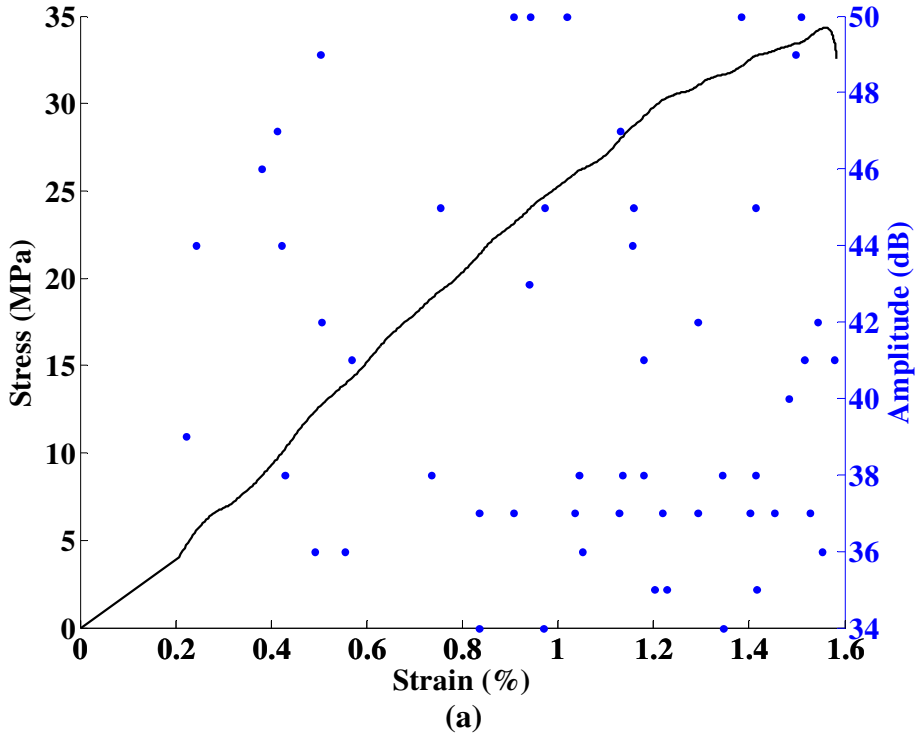

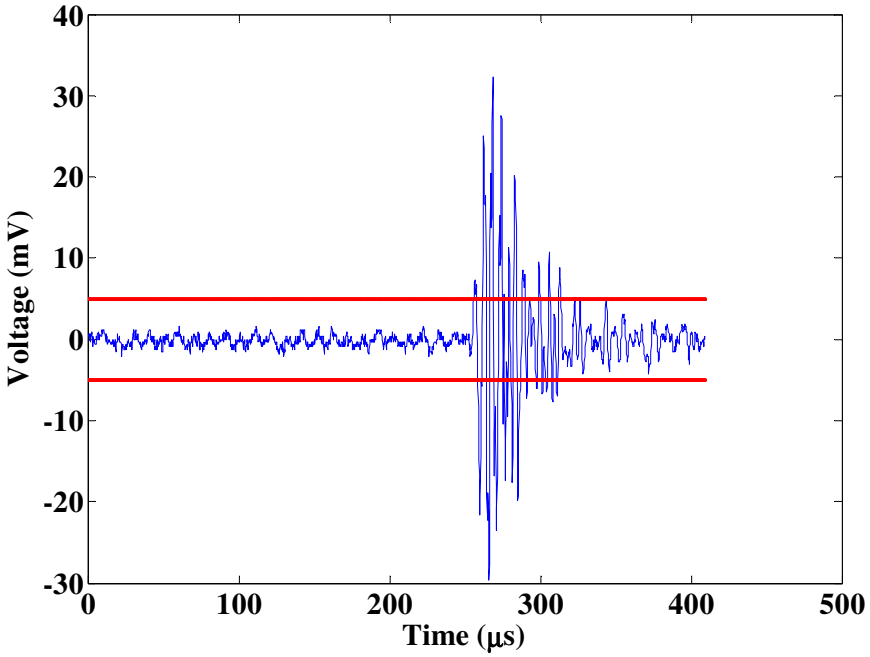

Fig.10. (a) Mechanical tensile curve coupled with the amplitude of AE activity recorded on pure resin sample; (b) waveform of the "**A**" signal marking the matrix cracking.

b. UD [90]$_4$ GFRP samples

Five monotonic tensile tests were conducted on the UD [90]$_4$ GFRP specimens with monitoring of their acoustic emission. **Fig.11** shows their typical tensile curve and the associated acoustic emission amplitude and number of cumulative counts. The dense and continuous acoustic activity started from a strain of 0.126%. The amplitude of the majority of the AE hits is between 45 dB and 55 dB, and that very few hits have an amplitude greater than 60 dB.

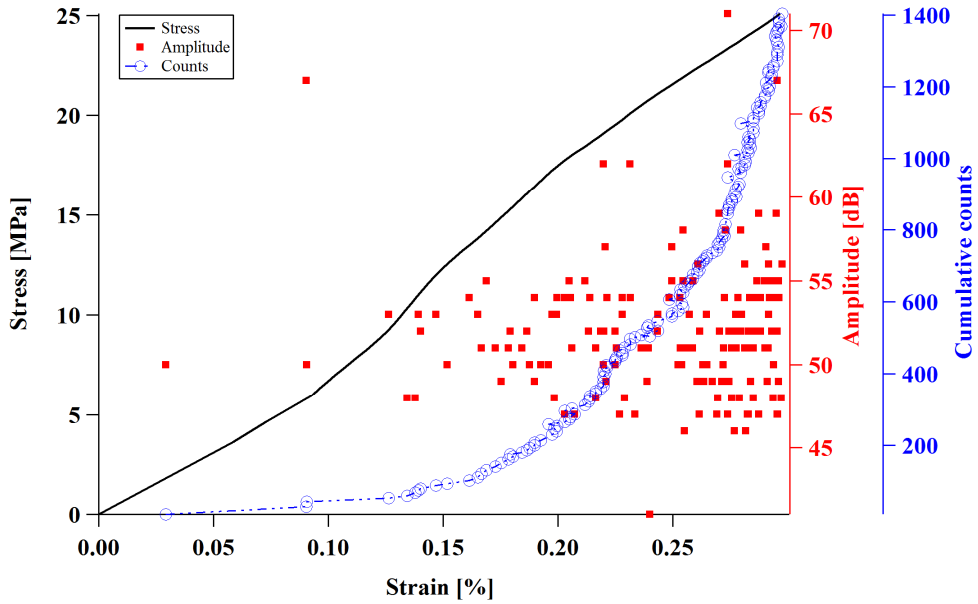

Fig.11. Typical tensile curve and acoustic emission activity in a UD $[90]_4$ GFRP specimen.

The correlation between the AE amplitude and duration of the hits is shown in **Fig.12**a. Almost all of the events are concentrated in the same group except two of them (hits No. 2 and 99) which have a duration greater than 300 µs. This type of representation can give a priori information on the number of damage mechanisms developed in the material, here 2. This estimation is consistent with the fact that UD $[90]_4$ composite could generate two damage mechanisms under uniaxial tensile stress, mainly matrix cracking and secondarily the interfacial debonding between fibers and matrix [28]. The weaker the fiber/matrix interface, the more the interfacial debonding mechanism becomes favored; this is closely related to the sizing, the manufacturing process, the material type and the applied mechanical stress. The obtained eigenvalues, following the PCA application on the four relevant descriptors of the AE data recorded on the UD $[90]_4$ sample, are the variances of the principal components. **Table 4** presents these variances (λ), their percentages (λ%) and their cumulative percentages (λcum%). The first two eigenvalues cumulate more than 80% of the total variance; therefore, they alone are sufficient to describe all the data. Thus, **Fig.12**b illustrates, in the principal component basis {1st principal component, 2nd principal component}, the result of k-means classification applied on the reduced centered data with a number of classes *K=2* minimizing the *DB* criterion. Thanks to this illustration, the two classes are easily distinguished with a contribution of 98.8% for the first one (red dots) and 1.2% for the second class corresponding to the two hits (N° 2 and 99, with two blue asterisks).

Table 4. Eigenvalues λ of the principal components, their percentages (λ%) and their cumulative percentages (λcum %)

Descriptors	**Rise time**	**Counts**	**Amplitude**	**Absolute energy**
λ	2.5169	0.8786	0.3705	0.2341
λ %	62.92	21.96	9.26	5.86
λcum %	62.92	84.88	94.14	100

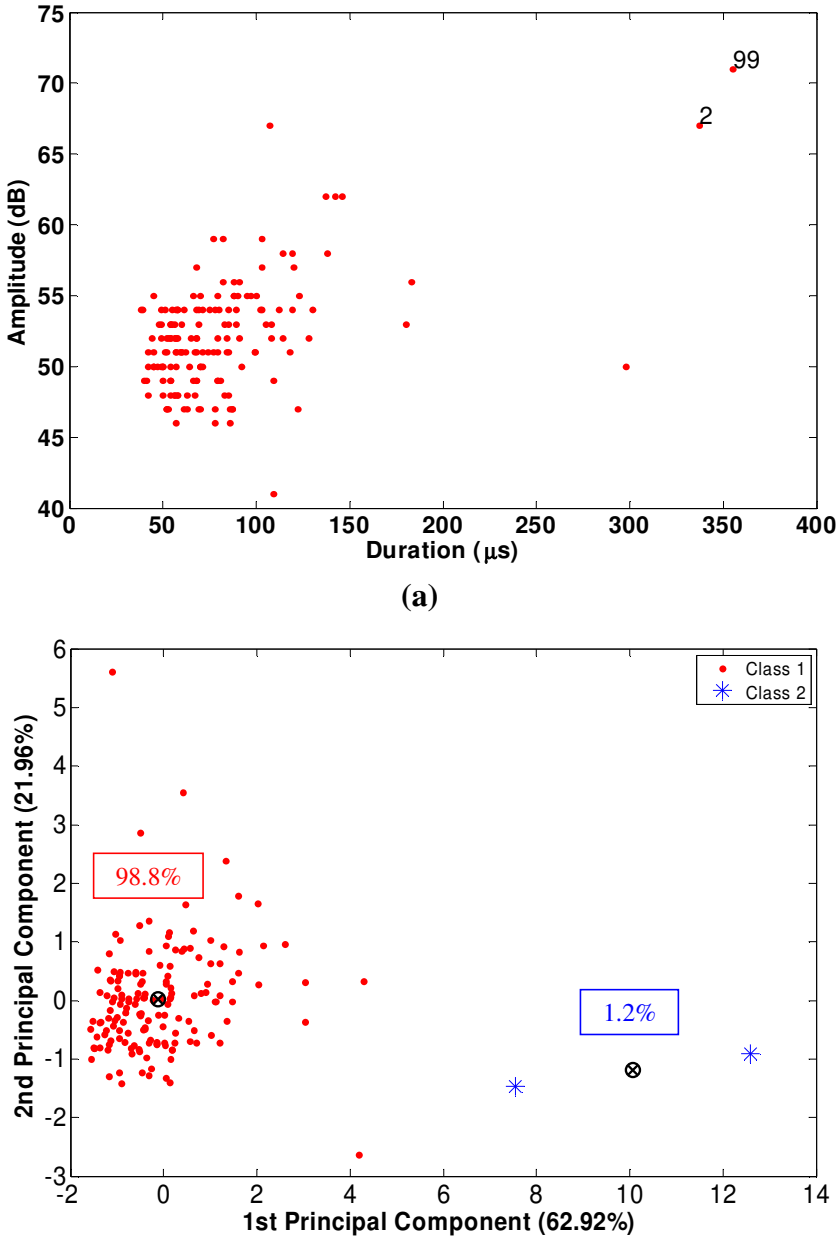

Fig.12. (a) Amplitude vs. duration, (b) PCA visualization of the k-means classification of the AE activity recorded on UD $[90]_4$ GFRP samples.

The averages of the pertinent parameters of the two obtained classes (class centers) are presented in **Table 5**. The values of the center of class 1 are quite similar to those previously identified on the pure resin sample describing matrix cracking. Thus, by deduction, the second class (class 2) describes the matrix/fiber debonding damage mechanism.

Table 5. Mean values of the pertinent parameters of the two obtained classes on UD $[90]_4$ PMC sample.

	Rise time (µs)	Counts	Amplitude (dB)	Absolute energy (aJ)
Class 1	18	9	52	158
Class 2	36	26	69	7023

The appearance chronology of the AE hits (**Fig.13**a) shows that class 1 (matrix cracking) happens first, before class 2 (fiber/matrix debonding). Also, the matrix cracking continues to

appear until the sample breakage, while the fiber/matrix debonding is stopped before. The waveforms corresponding to the two last damage mechanisms that occurred in the UD $[90]_4$ GFRP samples are presented in **Fig.13**b. The signal types "**B**" corresponding to the fiber/matrix debonding have a longer duration and higher amplitude in comparison with the matrix cracking (see also **Table 5**).

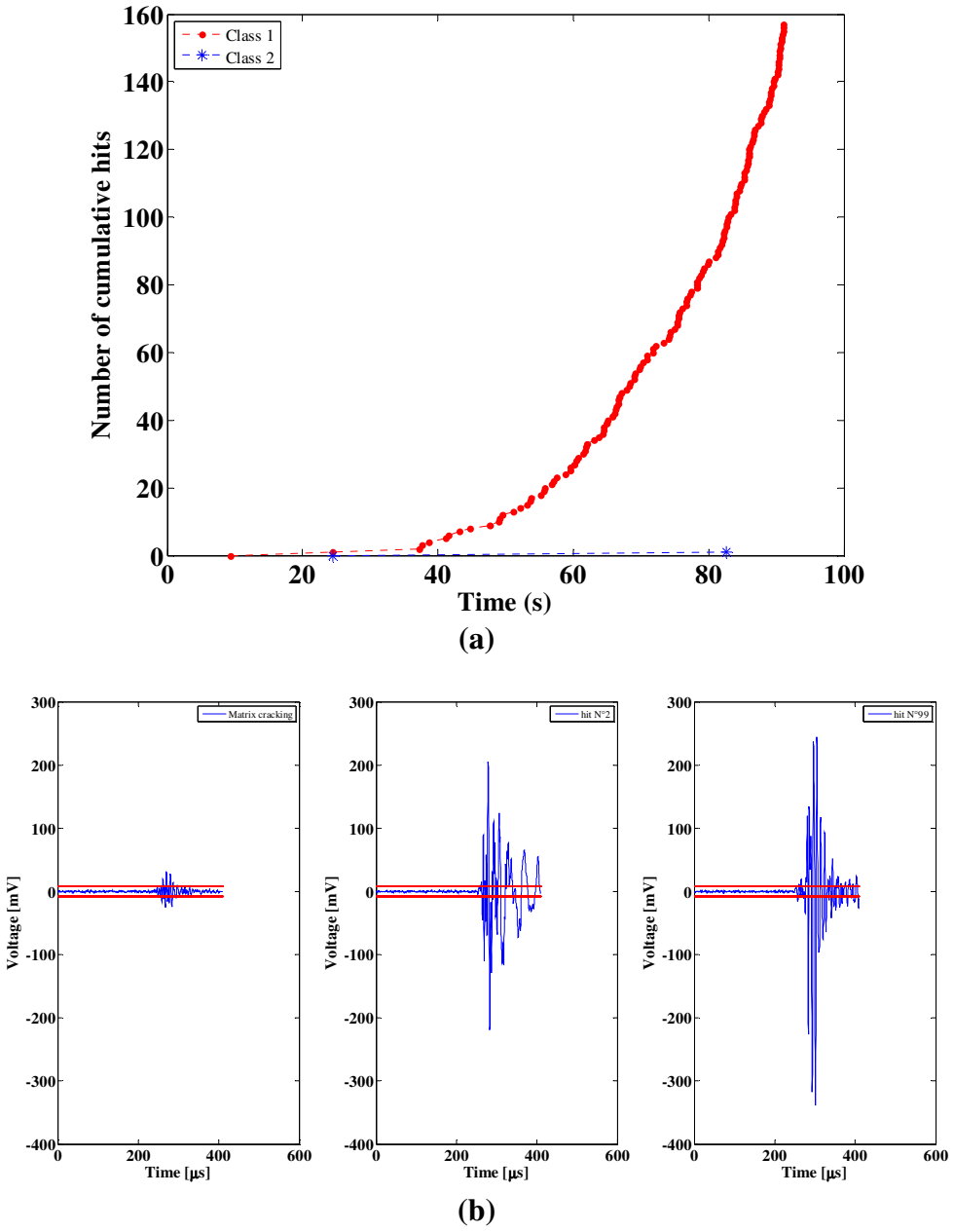

Fig.13. (a) Appearance chronology and (b) signal waveforms of the two damage mechanisms recorded on the UD $[90]_4$ PMCs.

c. UD $[0]_4$ GFRP samples

The typical tensile mechanical curve of the UD $[0]_4$ composite samples with the associated AE amplitude is presented in **Fig.14**a. A quasi-linear mechanical behavior is shown in comparison with the previous samples UD $[90]_4$ and pure resin. For UD $[0]_4$, the fibers strongly support the parallel applied load. Concerning the acoustic emission activity, two regimes are globally observed. The first one is comprised between 40 and 70 dB, starting from a very low strain ε = 0.035% and continuing with the same appearance density until the sample breakage. A second

regime (amplitude greater than 70 dB) starts from the strain ε = 0.55% with a weak density than the previous one and continues until the final rupture of the sample. The start stage of the second regime coincides with the first jump of the elongation, indicating probably the beginning of the fiber rupture. To better highlight this agreement between the strain jumps (the dropouts) and the fiber breakage, **Fig.14**b presents the cumulative released acoustic energy versus the mechanical strain. Four strain jumps are counted coinciding with four jumps in acoustic energy indicating the strong released energy when the fibers break.

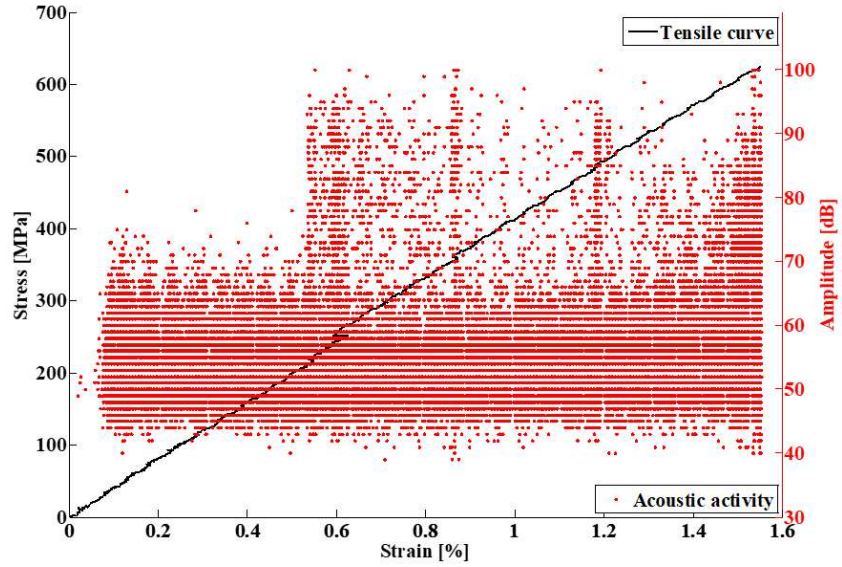

(a)

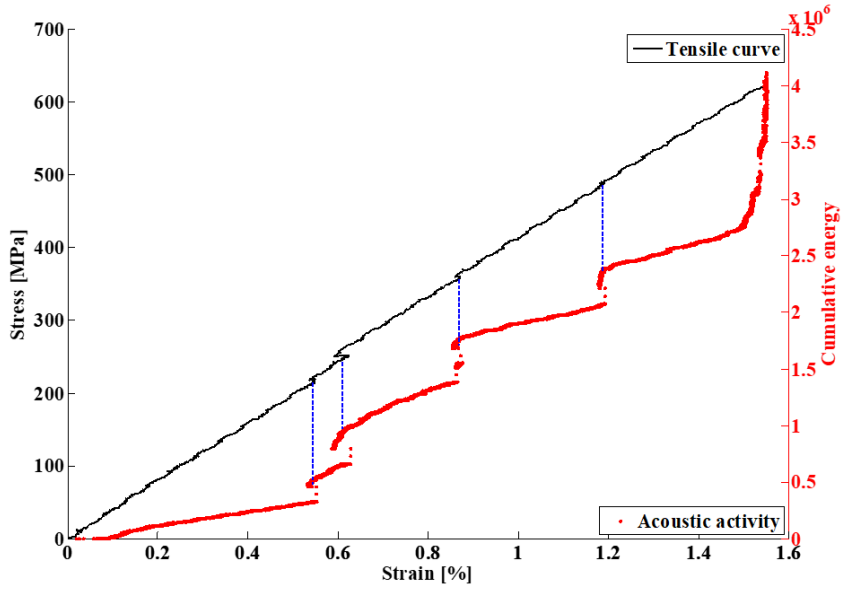

(b)

Fig.14. (a) Tensile curve with AE amplitude vs. strain; (b) Tensile curve with cumulative energy of the AE hits vs. strain obtained during a tensile test of UD $[0]_4$ GFRP.

Fig.15a shows the classification of the AE data, recorded on the UD $[0]_4$ sample, by applying k-means in their principal component basis. Matrix cracking (class 1) represents 94% of the acoustic emission activity, while fiber breakage (class 3) contributes with just 6%. Indeed, this labeling of the two classes is confirmed by relying on the associated relevant parameters presented in **Table 6**, and a priori knowledge of the matrix cracking signature. The descriptors

of the fiber breakage are much more different than those observed for the matrix cracking and fiber/matrix debonding.

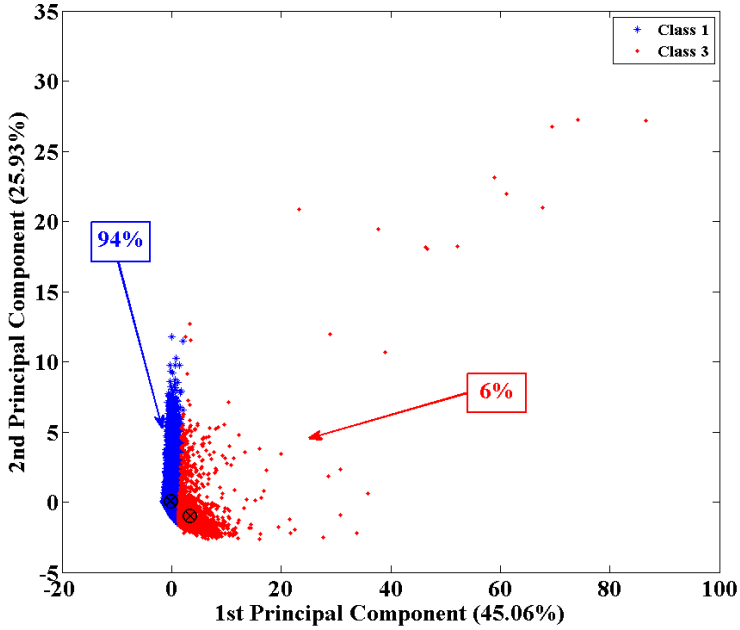

(a)

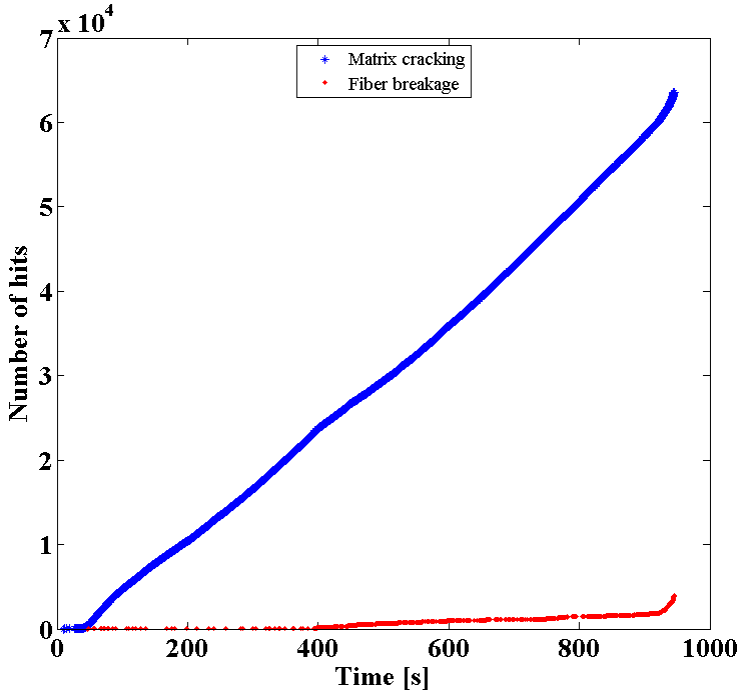

(b)

Fig.15. (a) PCA visualization of the k-means classification result; (b) Appearance chronology of matrix cracking and fiber breakage within a UD $[0]_4$ samples.

Table 6. Average values of the pertinent parameters of the two obtained classes on UD $[0]_4$ GFRP sample.

	Rise time (µs)	**Counts**	**Amplitude (dB)**	**Absolute energy (aJ)**
Class 1	14	13	54	336
Class 3	15	162	78	797354

The appearance timeline of the AE hits, illustrated in **Fig.15**b, states that the matrix cracking occurs before the fiber breakage, knowing that the earliest fiber breakages correspond to blunt fibers. The two mechanisms continue to progress together until the final rupture of the sample. The typical waveforms corresponding to these two damage mechanisms are illustrated in **Fig. 16**. The matrix cracking is characterized, as in the case of UD $[90]_4$ samples, by its resonant waveform (signal "**A**") while the breaking of the fibers takes a rather impulse shape with high amplitude, long duration and a very short rise time (signal "**C**").

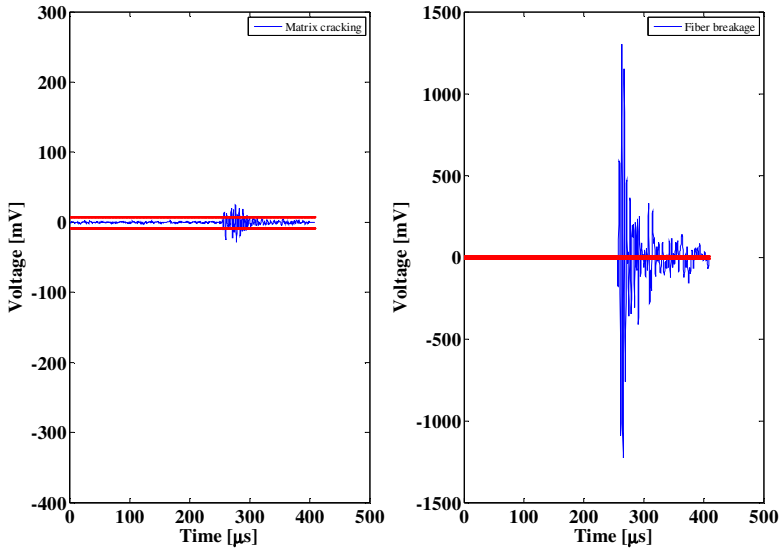

Fig. 16. Waveforms of the two damage mechanisms recorded on the UD $[0]_4$ samples: matrix cracking (on the left) and fiber breakage (on the right).

4.1.2. Mechanical and acoustic coupling on the cross-ply GFRP specimens

Since the acoustic signatures of the three damage mechanisms are known, namely matrix cracking, fiber/matrix debonding and fiber breakage, the one corresponding to delamination appearing relatively easily in the laminated GFRPs can be identified by deduction. To achieve this, monotonic tensile tests were carried out on five cross-ply $[0/90]_S$ samples. **Fig.17**a shows the typical tensile curve of these samples with associated AE amplitude. The acoustic activity is very dense in this latter case compared to the previously studied UD samples. A remarkable strain jump happened at $\varepsilon = 1.57\%$ strain indicating the creation of strong damage in the material. In order to identify the acoustic signature of the fourth mechanism, which is delamination between the plies of the $[0/90]_S$ laminate, the k-means algorithm is applied to the recorded AE data while assuming that the number of classes is equal to 4. **Fig.17**b shows the result of this classification, where the contributions from classes 1, 2, 3 and 4 are respectively 78.8%, 5.9%, 15% and 0.3%. The average values of the pertinent parameters of the four obtained classes are presented in **Table 7**. Based on these values as well as those previously determined for matrix cracking, fiber/matrix debonding and fiber breakage, class 4 is identified and associated to the delamination mechanism (0.3%).

Table 7. Average values of the pertinent parameters of the four obtained classes on cross-ply $[0/90]_S$ GFRP sample.

	Rise time (µs)	**Counts**	**Amplitude (dB)**	**Absolute energy (aJ)**
Class 1	11	5	45	52.23
Class 2	74	32	57	94.69×10^3
Class 3	22	46	71	220.5×10^3
Class 4	83	780	99	9015×10^4

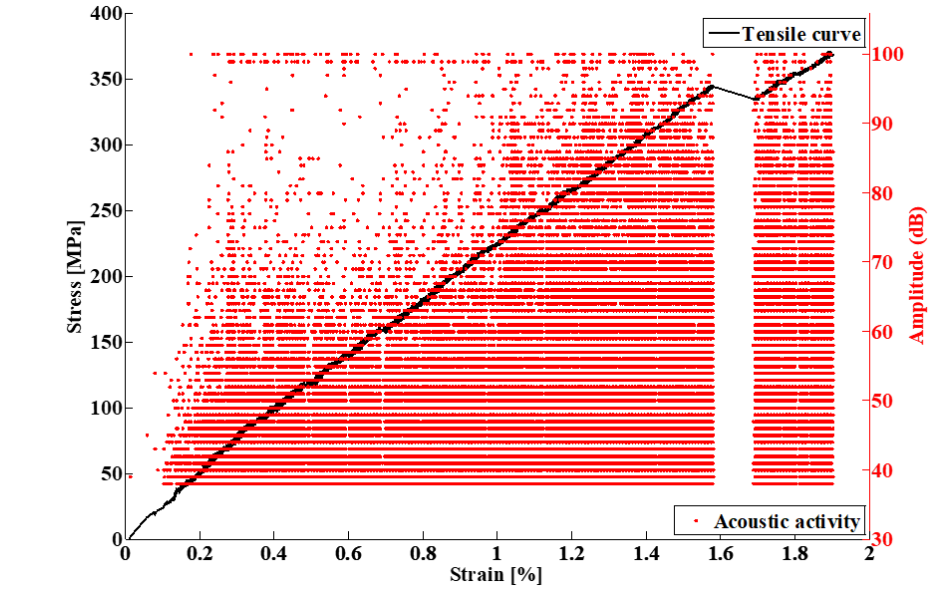

(a)

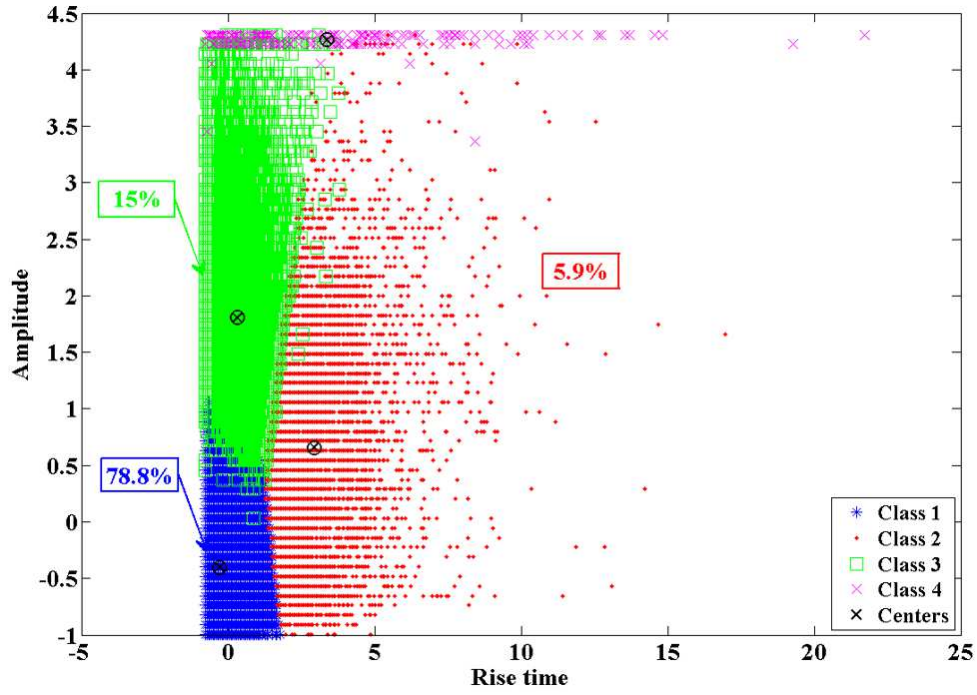

(b)

Fig.17. (a) Tensile curve with AE amplitude vs. strain; (b) k-means classification result of AE data recorded on a cross-ply $[0/90]_S$ specimen.

Fig.18a shows the appearance chronology of the damage mechanisms, which is deducted from the evolution curves of the number of cumulative hits for each class. According to these curves, the order of appearance of the classes is as follows: class 1 (matrix cracking), class 2 (fiber/matrix debonding), class 4 (delamination) and class 3 (fiber breakage). This chronology is logical and expected for this type of material (laminate $[0/90]_S$), where the plies oriented at 90° are the first damaged, hence the matrix cracking followed by fiber/matrix debonding and some blunt fiber breaks. Then, the delamination between the 0/90 plies occurs just before the ultimate fibers breakage leading to failure. The waveforms corresponding to these four damage mechanisms, appearing in the $[0/90]_S$ GFRP material during a monotonic tensile test, are

presented in **Fig.18**b. Delamination is characterized by a very resonant signal (type "**D**"), of long duration, high amplitude and a very slow decay time.

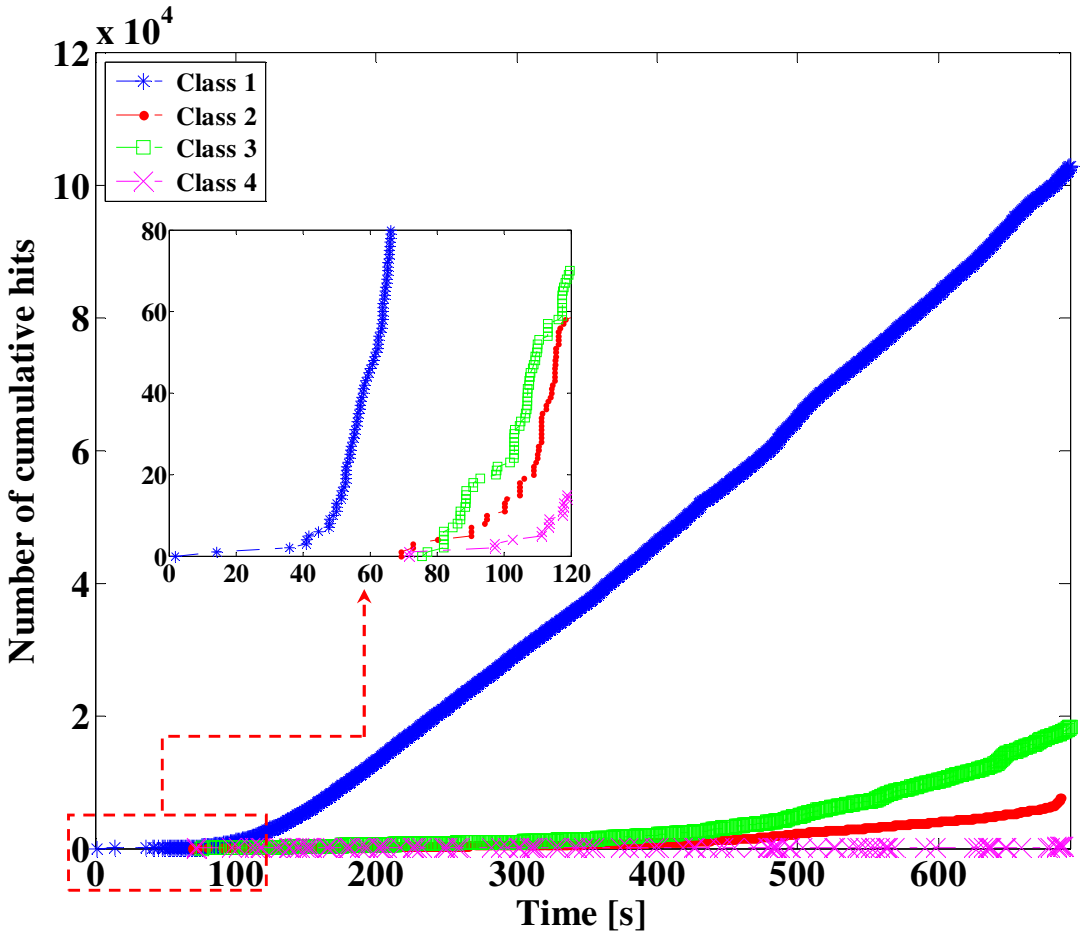

(a)

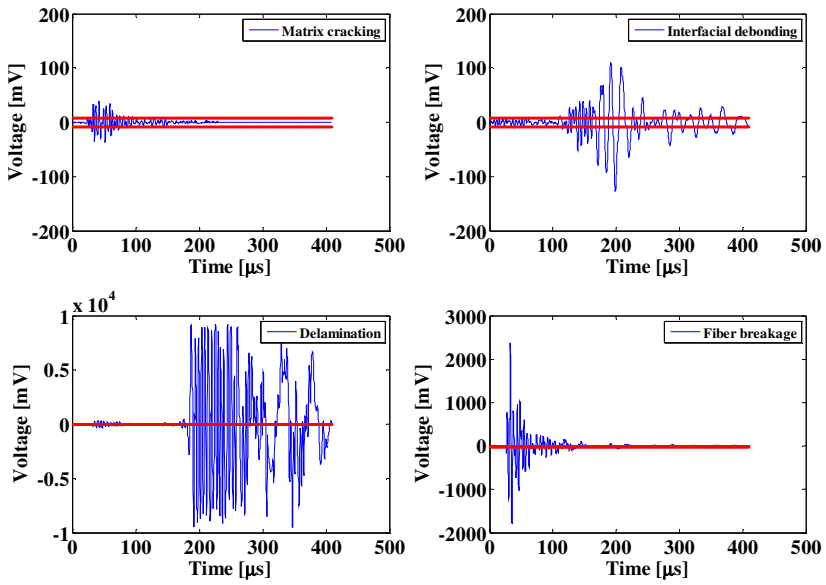

(b)

Fig.18. (a) Appearance chronology and (b) signal waveforms of the four damage mechanisms recorded on the $[0/90]_S$ PMCs.

4.1.3. SEM observations

The fracture surfaces of all pure resin, $[0]_4$, $[90]_4$ and cross-ply $[0/90]_S$ samples are inspected using SEM. **Fig.19**a shows the matrix cracks propagating throughout the thickness of the pure resin sample. On the $[90]_4$ GFRP specimen, the fracture surface (**Fig.19**b) shows the matrix crack initiation around the porosities and its propagation along the fibers oriented at 90° against of mechanical loading direction. The existence of streaks at 90° marks the pull-out mechanism when the glass fibers are torn from the epoxy matrix. It is important to highlight, that even after the pull-out, the fibers remain coated with their matrix, this confirms the majority contribution of matrix cracking compared to interfacial debonding on the $[90]_4$ material. Fractographic analysis of the cross-section of the UD $[0]_4$ sample (**Fig.19**c) highlights the matrix cracks surrounding the rupture of glass fibers. Finally, the four damage mechanisms are coexisting within the $[0/90]_S$ specimen with a clear delamination appearance between the layers oriented at 0° and 90°. Therefore, the fractographic analysis validates the acoustic emission identification of all damage mechanisms occurring in the tested GFRP materials under tensile loading.

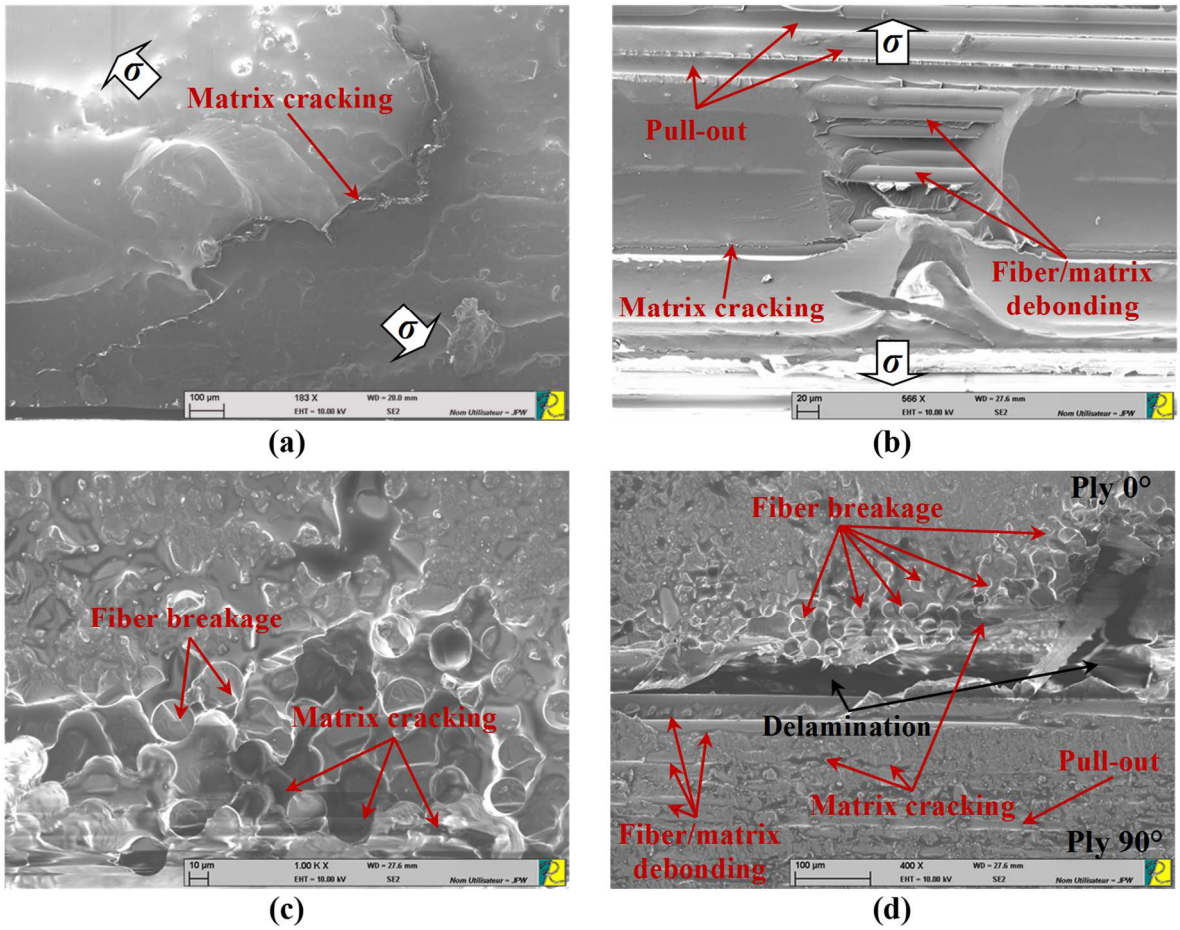

Fig.19. SEM analysis conducted on the (a) pure resin, (b) $[90]_4$, (c) $[0]_4$ and (d) cross-ply $[0/90]_S$ fracture surfaces.

4.2. Identification of the cross-ply GFRP damages according to the applied stress: application of KSOM during loading (2)

The fact that the acoustic signatures of the four damage mechanisms, liable to appear in the $[0/90]_S$ laminated GFRP material under mechanical tensile stress, are now known, thus they can be used to characterize the overall damage of this material according to the level of the applied stresses. To achieve this, the $[0/90]_S$ samples are submitted to a step-wise tensile test

of 50 MPa loading ramps. The real applied mechanical loading (showing some unintended hooks/decreases of the applied stress due to occurred damage), as well as its associated acoustic emission activity, are presented in **Fig.20**a. In total, seven loading steps and six levels of holding at constant stress were applied. The acoustic emission activity begins from the start of the loading with low amplitudes concentrated between 38 dB and 50 dB. It becomes increasingly denser, where 90% of the AE activity is recorded during the two last loading steps, with the appearance of high acoustic amplitudes as the loading level increases. The number of the recorded hits during each loading shows the accentuation of the damage at the end of the mechanical test (see **Fig.20**a, **Table 8**).

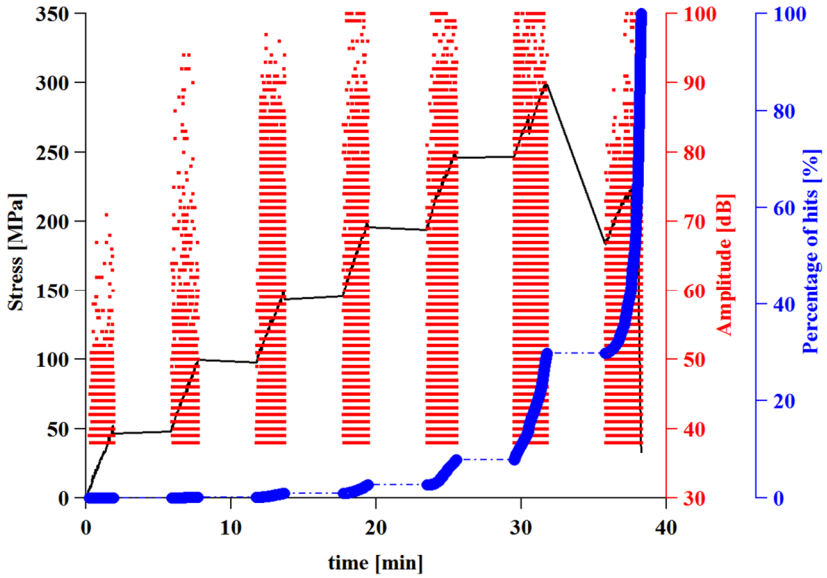

(a)

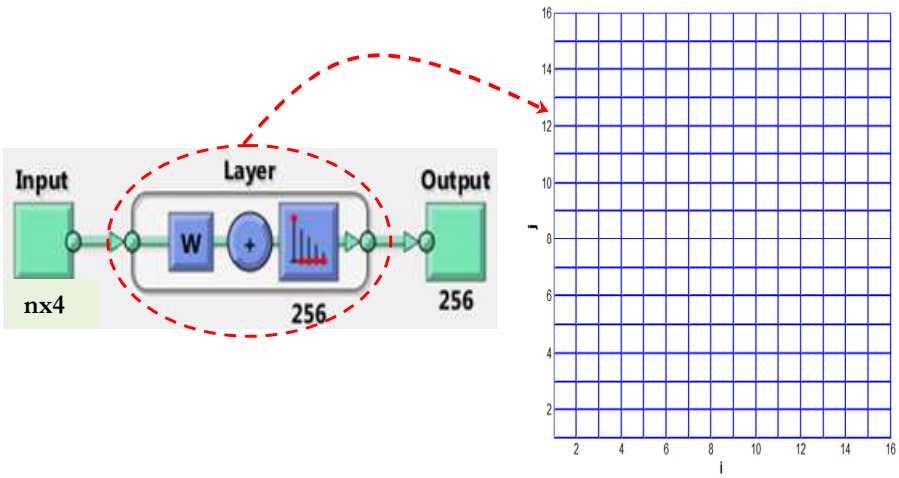

(b)

Fig.20. (a) Applied mechanical loading with its associated acoustic emission activity in terms of amplitude and percentage of recorded hits; (b) KSOM of 256 (16×16) neurons used for the classification of AE data recorded during mechanical loading (2) [42].

Table 8. Number of hits recorded during each loading step of the mechanical loading (2).

Number of loading ramp°	Number of hits "*n*"
1	1846
2	2518
3	6550

4	7379
5	13132
6	29646
7	50836

The applied KSOM uses the "Neural network toolbox" module of Matlab® software (**Fig.20**b, [42]). This map has the advantage of being "objective" for the classification of AE data because it does not require any a priori indication of the number of classes to be obtained. The input data of the map are the "*n*" AE hits recorded during each loading step (**Table 8**) and described by the four pertinent descriptors (rise time, number of counts, amplitude and absolute energy) introduced in the reduced centered form. The choice of the map topology (number of neurons) has been empirically optimized since there is no specific rule to satisfy. The optimization consisted of increasing the number of neurons step by step until a stable classification result was obtained (increasing the number of neurons more than enough will only increase unnecessarily the computing time). The chosen map is flat with 256 neurons distributed according to a 16×16 rectangular grid (**Fig.20**b). Each neuron is represented by its coordinates *i* and *j*. At the output of the used KSOM, the classification result will be in the form of neural groupings illustrating the number of AE hits that have been allocated to each elected or winning neuron *q** (so, these hits will be noted **hits***). This classification requires three steps after the creation of the network: learning the neurons, labeling of the different zones of the map, and finally, the use of the map for the identification of the damage mechanisms generated during each loading step.

4.2.1. Learning of neurons

The learning task is described in section 2.3. Training data are extracted from the AE signals recorded during the mechanical loading (1) applied on the $[0/90]_S$ laminated samples. This dataset is injected into the map to initialize the weight vectors of the 256 neurons, so groupings of similar AE hits* are established. The result of this learning is shown in **Fig.21**. To identify the different zones of this learned map, the labeling stage must be conducted.

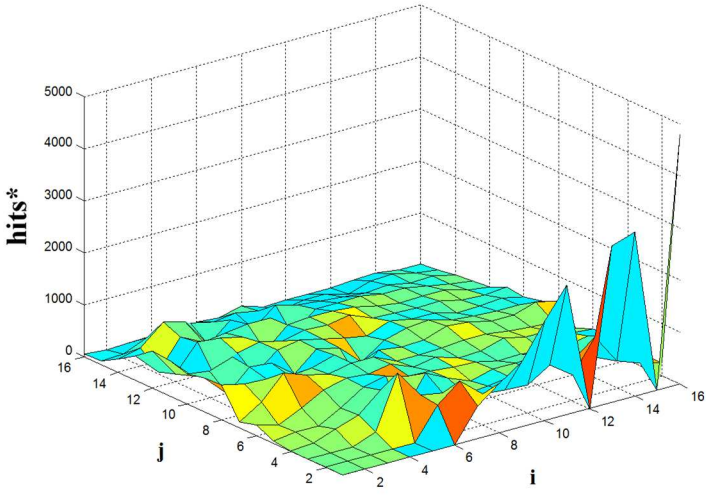

Fig.21. Learning result of the KSOM using different AE data recorded on the $[0/90]_S$ samples during the mechanical loading (1).

4.2.2. The labeling step

It consists of assigning "labels", that is to say, names, to the different neural groupings obtained after the learning phase. For this, the results of the k-means classification illustrated in **Fig.17**b are exploited. The idea is to activate the Kohonen map by injecting the data of the classes

identified by k-means one by one. The principle and the results of this operation are shown in **Fig.22**. This labeling procedure made it unambiguously possible to "label" all areas of Kohonen's map given by the learning operation. Thus, this self-organizing map can be used as a classifier of the AE data recorded during each loading step of the mechanical loading (2) applied to the laminated $[0/90]_S$ samples (**Fig.20**a).

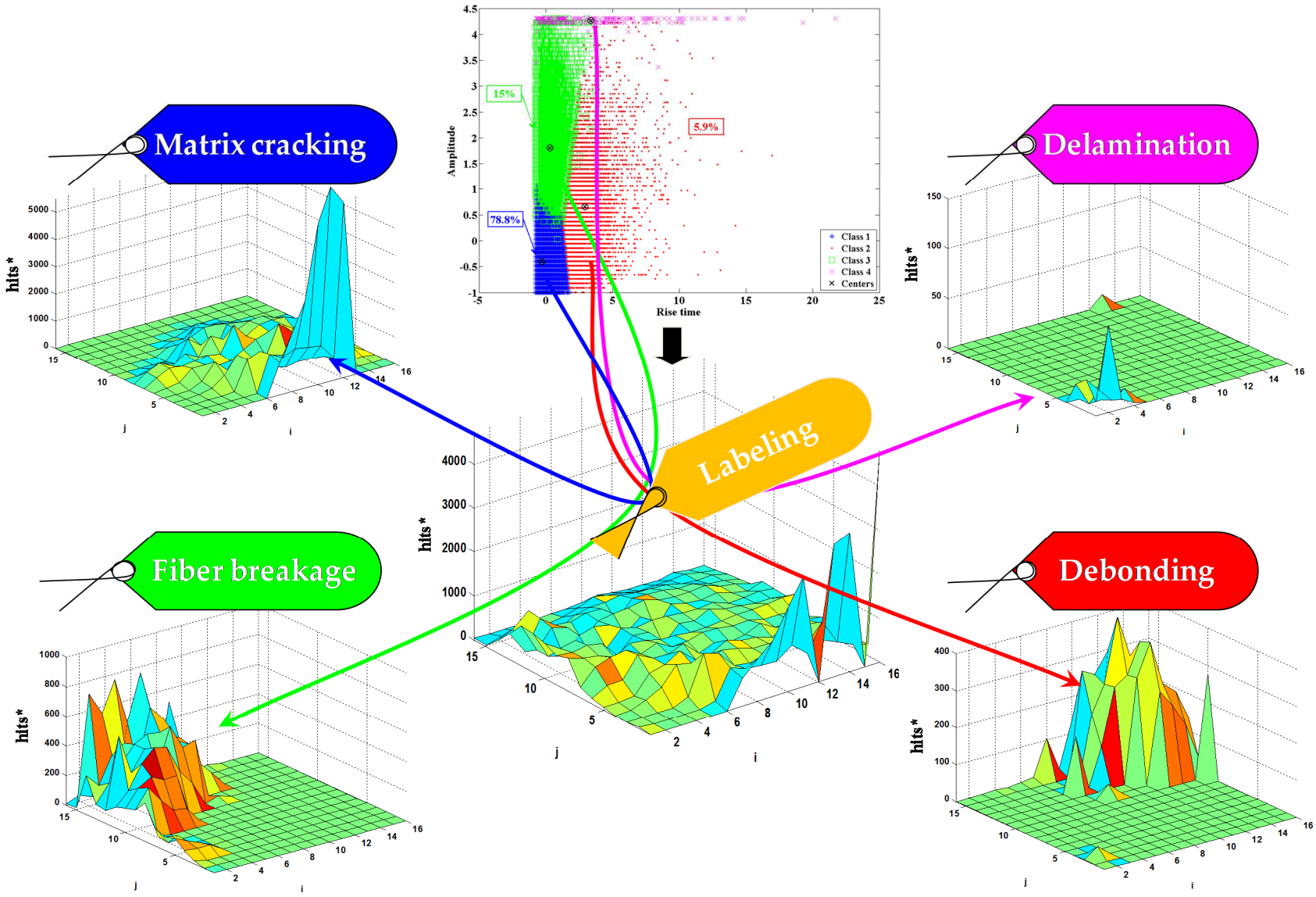

Fig.22. The labeling of the self-organizing map from the AE data recorded during loading (1).

4.2.3. Identification of the damage mechanisms according to the applied stress

To achieve this, the AE data corresponding to each loading ramp (7 in total, according to **Table 8**) were injected into the previously learned map. The results of this identification are shown in **Fig.23**a-g. For the two first loadings in which the number of hits is 1846 and 2518, respectively (**Table 8**), Kohonen's map reveals only the zone marking the matrix cracking (**Fig.23**a-b). From the third loading, **Fig.23**c, the matrix cracking, fibers/matrix debonding and the breakage of the fibers appear together on the map. The number of AE hits allocated to the fiber/matrix debonding is weak during loading 4 (**Fig.23**d). However, it is accentuated at the loading ramps 5 (**Fig.23**e) and 6 (**Fig.23**f). Finally, delamination was detected only in a small percentage during the three last loadings (**Fig.23**e, f and g). All in all, matrix cracking is the predominant mechanism, occurred in cross-ply $[0/90]_S$ GFRP samples, from the start of the test until the end.

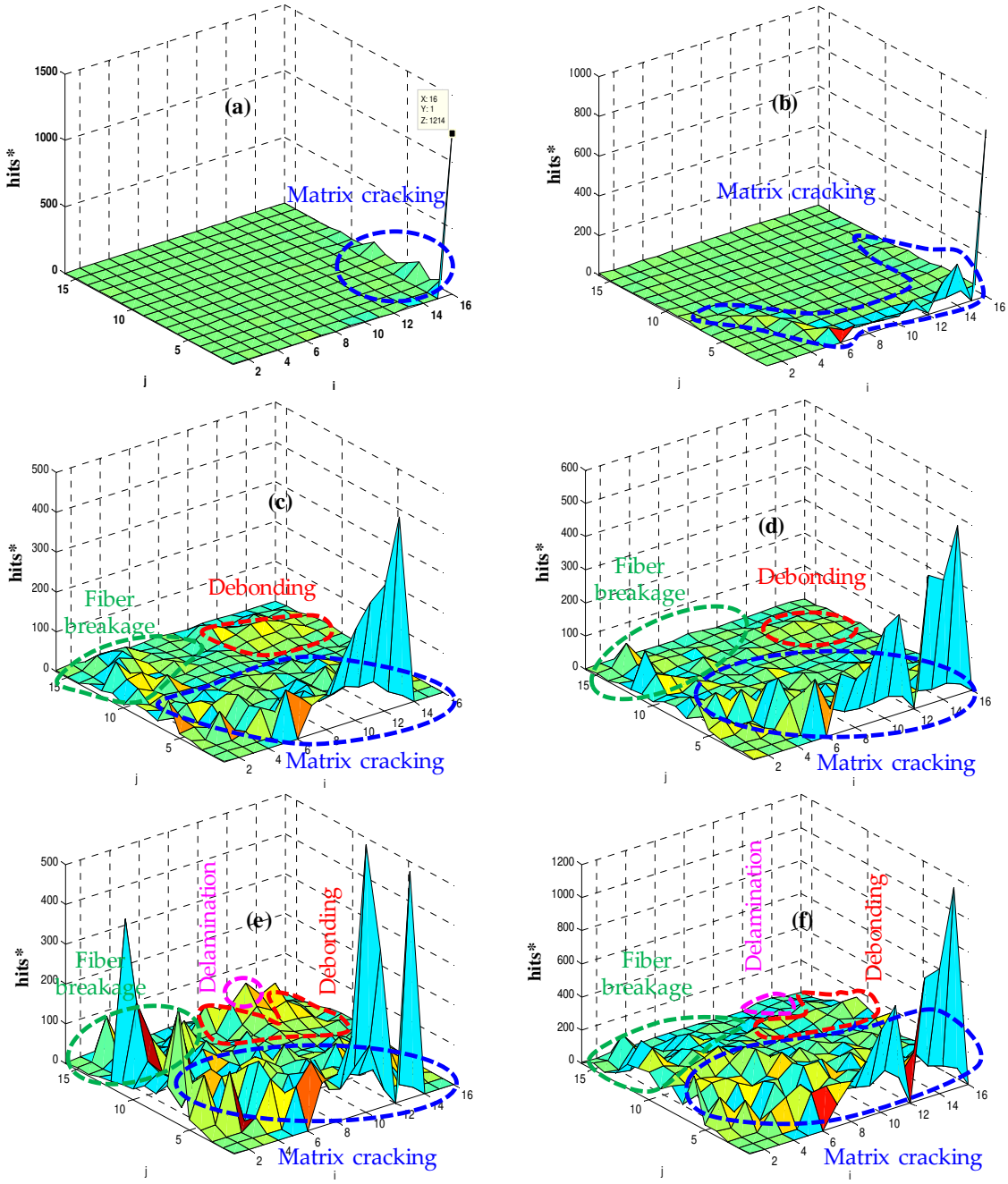

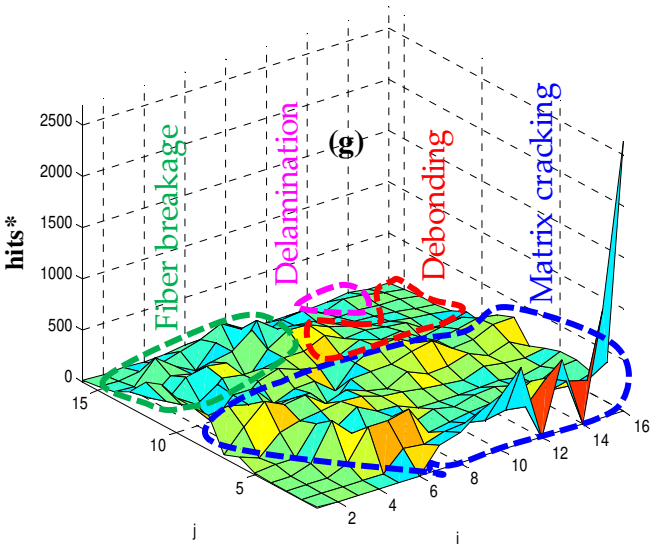

Fig.23. Classification of the AE data recorded during loading (2), according to the applied stress and using the self-organizing map: (a) ramp 1 at 50MPa, (b) ramp 2 at 100MPa, (c) ramp 3 at 150MPa, (d) ramp 4 at 200MPa, (e) ramp 5 at 250MPa, (f) ramp 6 at 300MPa, (g) ramp 7 at 350MPa.

5. Conclusions

The first objective of this study was to identify separately the acoustic signature of the four damage mechanisms occurring in $[0/90]_S$ GFRP materials when submitted to tensile loading, namely matrix cracking, fiber/matrix debonding, delamination and rupture of fibers. Once the acoustic signatures were identified, they were exploited to practice learning and labeling Kohonen's map, which in turn was used to characterize the damage of the laminate $[0/90]_S$ composite material under different loading conditions.

Achieving the first objective has involved manufacturing of typical specimens in pure epoxy resin, UD $[90]_4$, UD $[0]_4$, and finally, in laminate $[0/90]_S$ to characterize respectively the matrix cracking, the fibers/matrix debonding, the fiber breakage and the delamination mechanisms. The separation between these different mechanisms was allowed by a k-means classification algorithm using four pertinent descriptors (rise time, number of counts, amplitude and absolute energy). This preliminary acoustic emission study was validated with the post-mortem SEM observations carried out on the rupture facies of all the tested samples.

The obtained acoustic signatures were used subsequently to discriminate the damage mechanisms that occurred in the $[0/90]_S$ GFRP samples under a step-wise tensile test using Kohonen's self-organizing map.

All in all, the results of this study clearly showed the potential to use the acoustic emission technique for monitoring the damage occurring in composite materials during in-service loadings if their acoustic signatures had been characterized beforehand.

6. Data availability

The raw/processed data required to reproduce these findings cannot be shared at this time as the data also forms part of an ongoing study.

References

[1] Richard M. Christensen. Mechanics of Composite Materials. Mineola, New York: 2005.

[2] Harizi W. Caractérisation de l'endommagement des composites à matrice polymère par une approche multi-technique non destructive [Doctoral thesis]. Université de Valenciennes et du Hainaut Cambrésis, France, 2012.

[3] Harizi W, Monnin A, Aboura Z, Benzeggagh M. A New Hydraulic Crash Machine for Composite Structures. Journal of Dynamic Behavior of Materials 2015;1. https://doi.org/10.1007/s40870-015-0004-8.

[4] Harizi W, Kaidi S, Monnin A, el Hajj N, Aboura Z, Benzeggagh M. Study of the Dynamic Response of Polymer-Matrix Composites Using an Innovative Hydraulic Crash Machine. Journal of Dynamic Behavior of Materials 2015;1:359–69. https://doi.org/10.1007/s40870-015-0032-4.

[5] Berthelot J. Composite Materials, Mechanical Behaviour and Structural Analysis. New York, NY: Springer New York; 1999. https://doi.org/10.1007/978-1-4612-0527-2.

[6] Barré S, Benzeggagh ML. On the use of acoustic emission to investigate damage mechanisms in glass-fibre-reinforced polypropylene. Composites Science and Technology 1994;52:369–76. https://doi.org/10.1016/0266-3538(94)90171-6.

[7] Berthelot J. Relation between Amplitudes and Rupture Mechanisms in Composite Materials. Journal of Reinforced Plastics and Composites 1988;7:284–99. https://doi.org/10.1177/073168448800700306.

[8] Chaki, S., Harizi, W., Krawczak, P., Bourse, G., Ourak M. Structural health of polymer composites: non-destructive diagnosis using a hybrid NDT approach. JEC Composites Magazine 2016:62–5.

[9] Harizi W, Chaki S, Bourse G, Ourak M. Mechanical damage assessment of Polymer-Matrix Composites using active infrared thermography. Composites Part B: Engineering 2014;66. https://doi.org/10.1016/j.compositesb.2014.05.017.

[10] Harizi W, Chaki S, Bourse G, Ourak M. Mechanical damage assessment of Glass Fiber-Reinforced Polymer composites using passive infrared thermography. Composites Part B: Engineering 2014;59. https://doi.org/10.1016/j.compositesb.2013.11.021.

[11] Chaki S, Harizi W, Bourse G, Ourak M. Multi-technique approach for non destructive diagnostic of structural composite materials using bulk ultrasonic waves, guided waves, acoustic emission and infrared thermography. Composites Part A: Applied Science and Manufacturing 2015;78:358–61. https://doi.org/10.1016/j.compositesa.2015.08.033.

[12] Harizi W, Chaki S, Bourse G, Ourak M. Mechanical damage characterization of glass fiber-reinforced polymer laminates by ultrasonic maps. Composites Part B: Engineering 2015;70. https://doi.org/10.1016/j.compositesb.2014.11.014.

[13] Martins AT, Aboura Z, Harizi W, Laksimi A, Khellil K. Analysis of the impact and compression after impact behavior of tufted laminated composites. Composite Structures 2018;184:352–61. https://doi.org/10.1016/j.compstruct.2017.09.096.

[14] Martins AT, Aboura Z, Harizi W, Laksimi A, Khellil K. Structural health monitoring for GFRP composite by the piezoresistive response in the tufted reinforcements. Composite Structures 2019;209:103–11. https://doi.org/10.1016/j.compstruct.2018.10.091.

[15] Martins AT, Aboura Z, Harizi W, Laksimi A, Hamdi K. Structural health monitoring by the piezoresistive response of tufted reinforcements in sandwich composite panels.

Composite Structures 2019;210:109–17. https://doi.org/10.1016/j.compstruct.2018.11.032.
[16] Harizi W, Azzouz R, Martins AT, Hamdi K, Aboura Z, Khellil K. Electrical resistance variation during tensile and self-heating tests conducted on thermoplastic polymer-matrix composites. Composite Structures 2019;224:111001. https://doi.org/10.1016/j.compstruct.2019.111001.
[17] Bigaud J, Aboura Z, Martins AT, Verger S. Analysis of the mechanical behavior of composite T-joints reinforced by one side stitching. Composite Structures 2018;184:249–55. https://doi.org/10.1016/j.compstruct.2017.06.041.
[18] Harizi W, Anjoul J, Acosta Santamaría VA, Aboura Z, Briand V. Mechanical behavior of carbon-reinforced thermoplastic sandwich composites with several core types during three-point bending tests. Composite Structures 2021;262. https://doi.org/10.1016/j.compstruct.2021.113590.
[19] Idriss M, el Mahi A. Linear and nonlinear resonant techniques for characterizing cyclic fatigue damage in composite laminate. Composites Part B: Engineering 2018;142:36–46. https://doi.org/10.1016/j.compositesb.2017.12.058.
[20] Harizi W, Chaki S, Bourse G, Ourak M. Characterization of the damage mechanisms in polymer composite materials by ultrasonic waves, Acoustic Emission and InfraRed thermography. ECCM 2012 - Composites at Venice, Proceedings of the 15th European Conference on Composite Materials, 2012.
[21] Harizi W, Tuloup C, Aboura Z. Evaluation of the crosslinking steps of an unsaturated polyester resin during the infusion process of polymer-matrix composites using embedded PZT transducer. ESAFORM 2021. https://doi.org/10.25518/esaform21.2693.
[22] Tuloup C, Harizi W, Aboura Z, Meyer Y, Ade B, Khellil K. Detection of the key steps during Liquid Resin Infusion manufacturing of a polymer-matrix composite using an in-situ piezoelectric sensor. Materials Today Communications 2020;24. https://doi.org/10.1016/j.mtcomm.2020.101077.
[23] Duchene P, Chaki S, Ayadi A, Krawczak P. A review of non-destructive techniques used for mechanical damage assessment in polymer composites. Journal of Materials Science 2018;53:7915–38. https://doi.org/10.1007/s10853-018-2045-6.
[24] Tuloup C, Harizi W, Aboura Z, Meyer Y, Khellil K, Lachat R. On the use of in-situ piezoelectric sensors for the manufacturing and structural health monitoring of polymer-matrix composites: A literature review. Composite Structures 2019;215:127–49. https://doi.org/10.1016/j.compstruct.2019.02.046.
[25] Tuloup C, Harizi W, Aboura Z, Meyer Y, Khellil K, Lachat R. On the manufacturing, integration, and wiring techniques of in situ piezoelectric devices for the manufacturing and structural health monitoring of polymer–matrix composites: A literature review. Journal of Intelligent Material Systems and Structures 2019;30:2351–81. https://doi.org/10.1177/1045389X19861782.
[26] Roget J. Émission acoustique. Techniques de l'ingénieur, Traité Mesures et Contrôle 1990;R3200.
[27] Ono K. Trends of recent acoustic emission literature. Journal of Acoustic Emission 1994;12:177–98.
[28] Stéphane Huguet. Application de classificateurs aux données d'émission acoustique : identification de la signature acoustique des mécanismes d'endommagement dans les composites à matrice polymère [Doctoral thesis]. INSA de Lyon, France, 2002.

[29] Ceysson O, Salvia M, Vincent L. Damage mechanisms characterisation of carbon fibre / epoxy composite laminates by both electrical resistance measurements and acoustic emission analysis. Scripta Materialia 1996;34:1273–80. https://doi.org/10.1016/1359-6462(95)00638-9.

[30] Kim ST, Lee YT. Characteristics of damage and fracture process of carbon fiber reinforced plastic under loading-unloading test by using AE method. Materials Science and Engineering A 1997;234–236:322–6. https://doi.org/10.1016/s0921-5093(97)00226-8.

[31] Kotsikos G, Evans JT, Gibson AG, Hale JM. Environmentally enhanced fatigue damage in glass fibre reinforced composites characterized by acoustic emission. Composites Part A: Applied Science and Manufacturing 2000;31:969–77. https://doi.org/10.1016/S1359-835X(00)00014-2.

[32] Marec A, Thomas JH, el Guerjouma R. Damage characterization of polymer-based composite materials: Multivariable analysis and wavelet transform for clustering acoustic emission data. Mechanical Systems and Signal Processing 2008;22:1441–64. https://doi.org/10.1016/j.ymssp.2007.11.029.

[33] Ely, T.M.; Hill E v. K. Longitudinal splitting and fiber breakage characterization in graphite epoxy using acoustic emission data. Materials Evaluation 1995;53:1995.

[34] Barnes C, Ramirez G. Acoustic emission testing of carbon fiber composite offshore drilling risers. In: American Society for Nondestructive Testing Inc, editor. The Sixth International Symposium on Acoustic Emission from Composite Materials, San Antonio, Texas: 1998, p. 13–22.

[35] Godin N, Huguet S, Gaertner R, Salmon L. Clustering of acoustic emission signals collected during tensile tests on unidirectional glass/polyester composite using supervised and unsupervised classifiers. NDT and E International 2004;37:253–64. https://doi.org/10.1016/j.ndteint.2003.09.010.

[36] Marec A. Contrôle de santé des matériaux hétérogènes par émission acoustique et acoustique non linéaire : discrimination des mécanismes d'endommagement et estimation de la durée de vie restante [Doctoral thesis]. Université du Maine, France, 2008.

[37] Kharrat M, Placet V, Ramasso E, Boubakar ML. Influence of damage accumulation under fatigue loading on the AE-based health assessment of composite materials: Wave distortion and AE-features evolution as a function of damage level. Composites Part A: Applied Science and Manufacturing 2016;109:615–27. https://doi.org/10.1016/j.compositesa.2016.03.020.

[38] Kharrat M, Ramasso E, Placet V, Boubakar ML. A signal processing approach for enhanced Acoustic Emission data analysis in high activity systems: Application to organic matrix composites. Mechanical Systems and Signal Processing 2016;70–71:1038–55. https://doi.org/10.1016/j.ymssp.2015.08.028.

[39] Foulon A. Détermination de la signature acoustique de la corrosiondes composites SVR (stratifiés verre résine) [Doctoral thesis]. Université de Technologie de Compiègne, 2016.

[40] Johnson M. Waveform based clustering and classification of AE transients in composite laminates using principal component analysis. NDT and E International 2002;35:367–76. https://doi.org/10.1016/S0963-8695(02)00004-X.

[41] Moevus M, Godin N, R'Mili M, Rouby D, Reynaud P, Fantozzi G, et al. Analysis of damage mechanisms and associated acoustic emission in two SiCf/[Si-B-C] composites

exhibiting different tensile behaviours. Part II: Unsupervised acoustic emission data clustering. Composites Science and Technology 2008;68:1258–65. https://doi.org/10.1016/j.compscitech.2007.12.002.
[42] Math works incorporation. MATLAB software, version R2020b. 2020.
[43] ISO. NF EN ISO 527-4 - Plastiques - Détermination des propriétés en traction - Partie 4 : conditions d'essai pour les composites plastiques renforcés de fibres isotropes et orthotropes. 1997.
[44] Physical Acoustics Corporation, MISTRAS Holdings Group. Digital Signal Processing with AEwin, User's manual. vol. Rev 3. 2005.